A PDTPQx:$PC_{61}BM$ Blend with Pronounced Charge-Transfer Absorption for Organic Resonant Cavity Photodetectors – Direct Arylation Polymerization vs. Stille Polycondensation

*Tom Vandermeeren[a,b,c], Quan Liu[a,b,c], Sam Gielen[a,b,c], Dries Theunissen[a,b,c], Siebe Frederix[a,b,c], Melissa Van Landeghem[a,b,c], Zhen Liu[d], Niko Van den Brande[d], Jan D'Haen[a,b,c], Jochen Vanderspikken[a,b,c], Laurence Lutsen[a,b,c], Koen Vandewal[a,b,c], Wouter Maes[a,b,c]**

[a] Hasselt University, Institute for Materials Research (IMO), Agoralaan Building D, 3590 Diepenbeek, Belgium

[b] IMEC, Associated Lab IMOMEC, Wetenschapspark 1, 3590 Diepenbeek, Belgium

[c] Energyville, Thorpark, 3600 Genk, Belgium

[d] Vrije Universiteit Brussel, Physical Chemistry and Polymer Science, Pleinlaan 2, 1050 Brussels, Belgium

* *Corresponding author. E-mail address: wouter.maes@uhasselt.be*

Keywords: direct arylation polymerization; organic photodetectors; near-infrared; intermolecular charge transfer; optical cavities

Abstract. Because of their intriguing properties for optoelectronic applications, research on organic semiconducting polymers has steadily progressed over the past decades, yielding increasingly fine-tuned (hetero)aromatic polymer backbones. In this work, the push-pull copolymer PDTPQx is synthesized, both *via* Stille polycondensation and direct arylation polymerization (DArP), permitting comparison of the two procedures. Near-infrared organic photodetectors (OPDs) are constructed based on these different polymer batches in combination with $PC_{61}BM$, and their performance was investigated. From the current-voltage characteristics, it is clear that the DArP polymer-based devices outperform those prepared from the Stille polymers, both in terms of dark current density and external quantum efficiency (EQE), and therefore in terms of specific detectivity as well. The relatively high highest occupied molecular orbital energy level of PDTPQx, in combination with the clear charge-transfer absorption band observed for the DArP-based device, is beneficial for application in organic resonant cavity photodetectors. Such OPDs are prepared for the DArP PDTPQx:$PC_{61}BM$ (1:4) blends with 180 and 210 nm thick bulk heterojunction active layers. EQEs of 2.5% at 1016 nm and 1% at 1140 nm are achieved, with full-width-at-half-maximum peak responses of 44 and 45 nm, respectively, and detectivities of 2.24 x 10^{10} and 1.06 x 10^{10} Jones.

1. Introduction

Light-based technology has become one of the pillars of our digital society. The quest for new and innovative electronics continues to grow. In order to keep up with this ever-increasing need, the design of new as well as the optimization of known materials is required. Organic semiconducting polymers have attracted much attention due to their potential applications in flexible and wearable electronics. They show inherent softness, flexibility, low weight, adjustable optoelectronic properties through tailored design of the molecular structure, and low-cost, large-scale production possibilities.[1] The versatility of synthetic organic and polymer chemistry enables these materials to be tuned as such that they can be incorporated into diverse optoelectronic devices,[2] such as organic photovoltaics (OPVs)[3], organic light-emitting diodes (OLEDs)[4], organic photodetectors (OPDs)[5, 6] and organic field-effect or electrochemical transistors (OFETs or OECTs)[7, 8], emphasizing the role of chemical design in the performance of organic semiconductors.[9] Increasingly fine-tuned (hetero)aromatic polymer backbones are being explored as a consequence of their interesting properties, advancing research on

organic semiconducting polymers. Therefore, also the demand for convenient, reliable, and efficient synthetic routes toward these polymer backbones has increased.

High-performance π-conjugated polymers with well-defined structures are typically synthesized via a transition metal-catalyzed cross-coupling polycondensation such as Migita-Kosugi-Stille[10], Suzuki-Miyaura[11], Kumada-Corriu[12] and Negishi[13], amongst others. Although these cross-coupling reactions necessitate the functionalization of both coupling sites, they have developed into effective synthetic protocols for organic and polymer chemistry. Metal-promoted C−H activation toward C−C bonds has been changing the field of synthetic chemistry for over half a century now,[14] yet it has only recently been explored for the synthesis of π-conjugated polymers, a procedure more widely known as direct arylation polymerization (DArP). This protocol requires the pre-activation of only one coupling site (*i.e.* the aryl halide), circumventing the preparation of organometallic derivatives and the associated cryogenic air- and water-free reaction conditions,[15] yielding a major two-fold advantage. First, the material synthesis is significantly simplified, in this way potentially enabling to use monomers that are not compatible with organometallic functionalization.[15] Second, it further solidifies the position of organic electronics as less toxic, more environmentally friendly, and more sustainable than their inorganic counterparts.[16-18] Furthermore, DArP appeals for its atom economy, effectiveness (providing targets in fewer synthetic steps), generation of more benign byproducts, and decrease of the overall cost for the preparation of conjugated polymers.

Although a broad range of monomers are now readily polymerizable,[15] DArP is known to produce defects in the chemical structure. For instance, the reactivity of C−H bonds on (hetero)aromatic β-carbon atoms can result in branched or cross-linked polymer chains. This is often countered by using a low-dielectric solvent (for instance toluene, xylenes or tetrahydrofuran) to yield low-defect materials.[14] As for other metal-catalyzed cross-coupling polymerizations, also for DArP homocoupling is a factor to take into account.[14] All of these defects have a significant effect on the optical and electronic properties of conjugated polymers.[19-21] Although some fundamental understanding of different DArP reaction protocols has been established, more detailed insights will be required to truly enable a broad reach within the field or organic electronics.

Within the diversity of optoelectronic applications leaning on photoactive semiconducting polymers, the OPD field is receiving increased interest in recent years. To achieve (wavelength-selective) near-infrared (NIR) detectivity, beyond the limit of Si-based photodetectors (> 1000 nm), different strategies have been introduced.[5,6] One of these approaches is based on the integration of donor:acceptor thin films showing weak (but distinct) charge-transfer (CT) absorption into optical cavity devices.[22-25] Encouraging results have been achieved so far, but this has been limited to very few donor polymer backbones (notably PBTTT[23,25]), presumably due to the requirement of intimate mixing between the donor and acceptor material on a molecular scale to achieve strong CT absorption. Alternative conjugated polymers showing higher highest occupied molecular orbital (HOMO) energy levels and intimate mixing with suitable acceptors – to shift the CT absorption wavelength further into the NIR and enhance the external quantum efficiency (EQE), respectively – should be investigated to elucidate the limits of this approach and to formulate clear material design guidelines.

In this work, the donor-acceptor type copolymer PDTPQx is synthesized. The electron-rich dithieno[3,2-*b*:2′,3′-*d*]pyrrole (DTP) unit is a small ladder-type moiety commonly employed in conjugated organic oligomers and polymers for organic electronics.[26-30] On the other hand, the electron-poor quinoxaline (Qx) core is generally known for its easily modifiable structure, allowing to tune the electrical, optical, and morphological properties for both polymers and small molecules.[31-33] The combination of both units affords the unique PDTPQx polymer with a high HOMO energy level. The polymer is synthesized both *via* Stille polycondensation and DArP, permitting an interesting

comparison of the two. The high-HOMO characteristic of PDTPQx is desired for its application in organic resonant cavity photodetectors, as this decreases the energy of the intermolecular CT absorption of the polymer:$PC_{61}BM$ blend, with a concomitant redshift of the direct CT absorption into the NIR.[6, 22-25] Therefore, the DArP PDTPQx:$PC_{61}BM$ blend is well suited to implement into a resonant optical cavity device architecture. Using this type of OPD, wavelength selective photodetection up to 1140 nm is achieved.

2. Results and discussion

The DTP synthesis (**Scheme 1**) starts with the Buchwald-Hartwig amination cyclization reaction of the commercially available 3,3'-dibromo-2,2'-bithiophene (**1**) with dodecylamine. The long *N*-alkyl side chain on the DTP unit ensures good solubility of the intended polymer. Stannylation using *n*-butyllithium and trimethyltin chloride generates the distannylated DTP monomer **3**.[34] The quinoxaline synthesis (**Scheme 2**) starts with the alkylation of thiophene with 2-ethylbromohexane, providing the alkylated thiophene **5**. Next, a Friedel-Crafts acylation with oxalyl chloride is performed, producing diketone **6**. Parallel to these reactions, 4,7-dibromobenzo[*c*][1,2,5]thiadiazole is reduced to its corresponding diamine using sodium borohydride. Diamine **8** is condensed with diketone **6**, yielding the desired bromine flanked quinoxaline monomer **9**.[35]

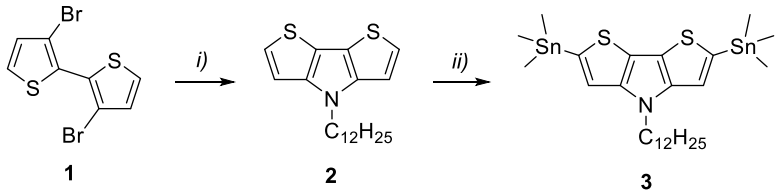

1 2 3

Scheme 1 Synthesis steps toward 4-dodecyl-2,6-bis(trimethylstannyl)-4*H*-dithieno[3,2-*b*:2',3'-*d*]pyrrole (**3**): *i*) dodecylamine, $Pd_2(dba)_3$, BINAP, sodium *tert*-butoxide, toluene, 120 °C (84%); *ii*) *n*-butyllithium, trimethyltin chloride, THF, -78 °C to RT (65%).

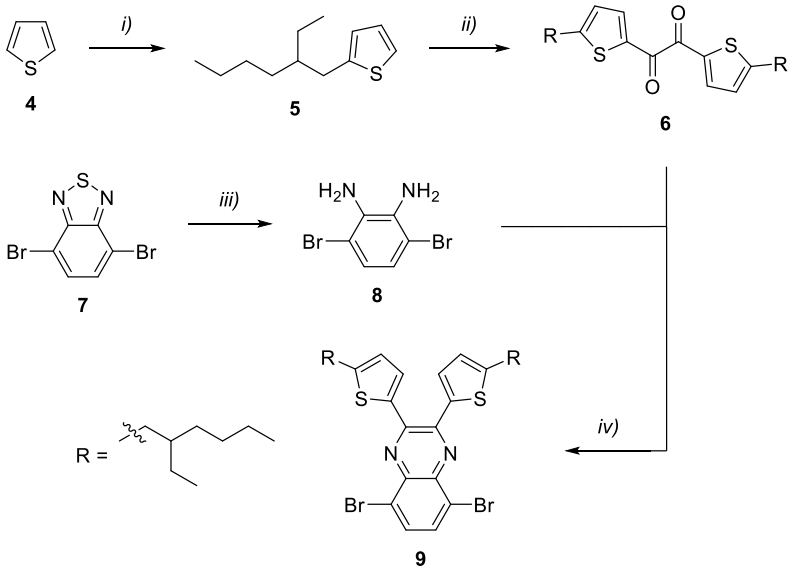

Scheme 2 Synthesis steps toward 5,8-dibromo-2,3-bis(5-(2-ethylhexyl)thiophen-2-yl)quinoxaline (**9**): *i*) *n*-butyllithium, KI, 2-ethylbromohexane, diethyl ether, -78 °C to RT (20%); *ii*) oxalyl chloride, $AlCl_3$, pyridine, dichloromethane, -20 °C to RT (24%); *iii*) $NaBH_4$, ethanol, RT (51%); *iv*) *p*-toluenesulfonic acid, methanol, reflux (73%).

The quinoxaline monomer **9** is then copolymerized with DTP monomers **2** and **3** *via* DArP and Stille polycondensation, respectively, yielding PDTPQx, as shown in **Scheme 3**. Two batches of PDTPQx are prepared via Stille polycondensation, referred to as 'Stille-L' and 'Stille-H' for the lower and higher molar mass batch, respectively. The only synthetic difference between the batches is the reaction time used and the amount of the catalytic system added. The PDTPQx batch prepared *via* DArP will simply be referred to as 'DArP'. The direct arylation polymerization reaction conditions are based on conditions reported by the Ozawa group, which were shown to inhibit branching and cross-linking.[36] All detailed reaction conditions are described in the supporting information (SI). All copolymers are purified by successive Soxhlet extractions, supplying the largest amounts from the dichloromethane fraction, indicating a high solubility of the PDTPQx polymers.

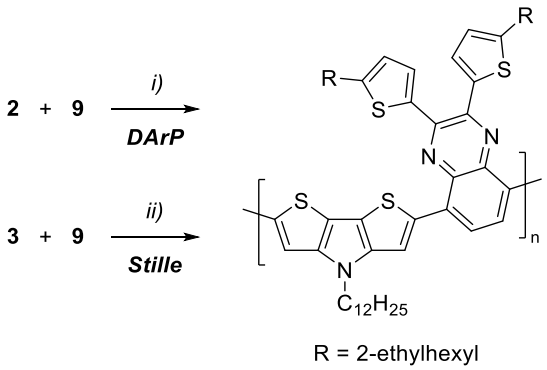

R = 2-ethylhexyl

Scheme 3 Synthesis steps toward PDTPQx *via* direct arylation polymerization (DArP) (*i*) and Stille polycondensation (*ii*): *i*) $Pd_2(dba)_3$, tris(*o*-anisyl)phosphine, Cs_2CO_3, pivalic acid, TMEDA, toluene, 100 °C; *ii*) $Pd_2(dba)_3$, tri(*o*-tolyl)phosphine, toluene:DMF (4:1), 120 °C.

All copolymers are then analyzed by high-temperature gel permeation chromatography (HT-GPC; **Figure S7**), yielding their molar masses and dispersities (Đ), shown in **Table 1**. The Stille-L and Stille-H batches have number average molar masses (M_n) of 12.7 and 27.1 kg mol^{-1} respectively, while the DArP fits right in between with a value of 19.9 kg mol^{-1}. This implies any difference observed in device performance at a later stage cannot solely be attributed to molar mass variation between the Stille and DArP materials (as it is known that higher molar mass polymers tend to give better device results).[37-39] Dispersities in the range of 2.2 to 2.6 are obtained. Cyclic voltammetry (CV) measurements are performed to estimate the frontier molecular orbital energy levels of the polymers (**Figure S8**). As expected, consistent energy level values are observed for all polymer samples, around -3.2 and -4.8 eV for the LUMO (lowest unoccupied molecular orbital) and HOMO, respectively. This is confirmed by the UV-Vis-NIR absorption spectra of the materials in solution and in film (**Figure 1**, **Figure S9**). The thermal properties of all polymer batches are studied *via* thermogravimetric analysis (TGA) and rapid heat-cool calorimetry (RHC). Mass loss is observed from *ca.* 400 °C for all polymer batches *via* TGA (**Figure S10**). RHC shows a very small melting peak for each polymer (**Figure S11**), even after using a cooling rate of 20 K min^{-1} to promote crystallization upon cooling, which exhibits a dependence on molar mass. Values for the peak maximum of the melting transition (T_m) and the melting enthalpy (ΔH_m) can be found in **Table 1**. For the lowest molar mass polymer Stille-L, the highest ΔH_m is observed, as well as a clearly broader melting peak with a more pronounced low-temperature contribution, and a lower T_m. The melting behavior of the Stille-H and DArP polymers is more similar, with a higher T_m for the higher molar mass Stille-H, and only a small difference in ΔH_m, indicating a similar degree of crystallinity. The observed dependence of melting behavior on molar mass may correspond to classical polymer crystallization, where extended chain crystals are formed at low molar mass and chain folding occurs at higher molar mass, as seen for *e.g.* poly(3-hexylthiophene).[38]

Table 1 Overview of the PDTPQx characterization data.

Polymer	M_n [a] (kg mol^{-1})	Đ [a]	$\lambda_{max,film}$ [b] (nm)	E_{red} [c] (V)	E_{ox} [c] (V)	E_{LUMO} [d] (eV)	E_{HOMO} [d] (eV)	$E_{g,opt}$ [e] (eV)	$E_{g,CV}$ [f] (eV)	T_m [g] (°C)	ΔH_m [h] (J g^{-1})
Stille-L	12.7	2.2	756	-1.68	-0.12	-3.22	-4.77	1.43	1.56	213	3.9
Stille-H	27.1	2.3	756	-1.67	-0.10	-3.22	-4.79	1.44	1.56	239	2.5
DArP	19.9	2.6	749	-1.67	-0.10	-3.23	-4.79	1.42	1.57	228	2.4

[a] Measured by HT-GPC at 160 °C in 1,2,4-trichlorobenzene. [b] Films were prepared by drop-casting a solution of the polymer onto a quartz disc. [c] Onset potentials *vs.* Fc/Fc$^+$. [d] Determined from the onset of oxidation/reduction in CV. [e] Optical bandgap, determined by the onset of the solid-state UV-Vis-NIR spectrum. [f] Electrochemical bandgap. [g] Melting transition peak maximum. [h] Melting enthalpy.

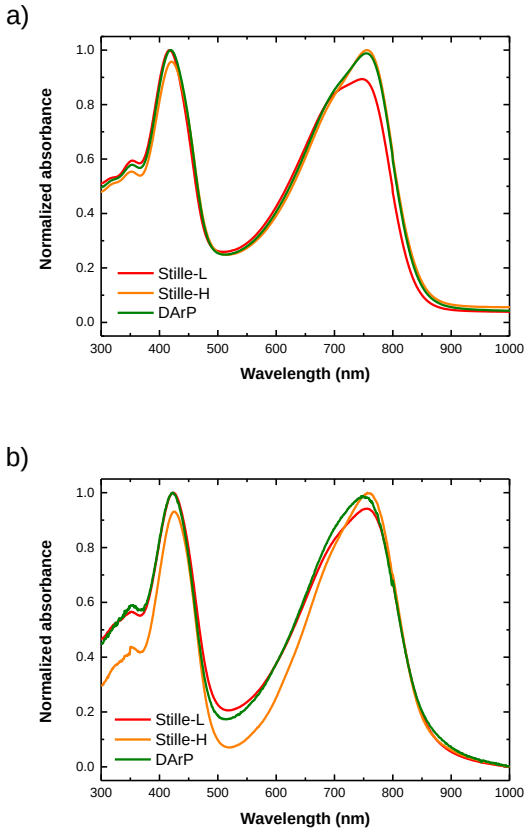

Figure 1 Normalized UV-Vis-NIR absorption spectra of PDTPQx in (a) solution and (b) drop-casted film.

The polymer structures are investigated in more detail *via* proton nuclear magnetic resonance (^{1}H-NMR) in *ortho*-dichlorobenzene-d_4 at 110 °C (**Figure S4-S6**). No major differences are observed between the polymers, except for somewhat better resolved signals for the lowest molar mass sample Stille-L. Therefore, matrix-assisted laser desorption/ionization - time-of-flight (MALDI-ToF) mass spectrometry is additionally applied (**Figure 2**). For all polymer batches, no mismatch in the amount of DTP and Qx building blocks is observed, pointing toward little or no homocoupling. In both Stille batches, the polymers show hydrogen, methyl, or both end groups. The methyl end groups are known to originate from the trimethylstannyl functionalization of the Stille monomer.[20] The DArP batch shows a main distribution with hydrogen end groups, but also two smaller distributions, either with one bromine or one tolyl end group. The major difference between the Stille and DArP polymers hence seems to be in their molar mass and end groups. Although the used DArP conditions should limit branching and cross-linking, this cannot be fully excluded either.[36]

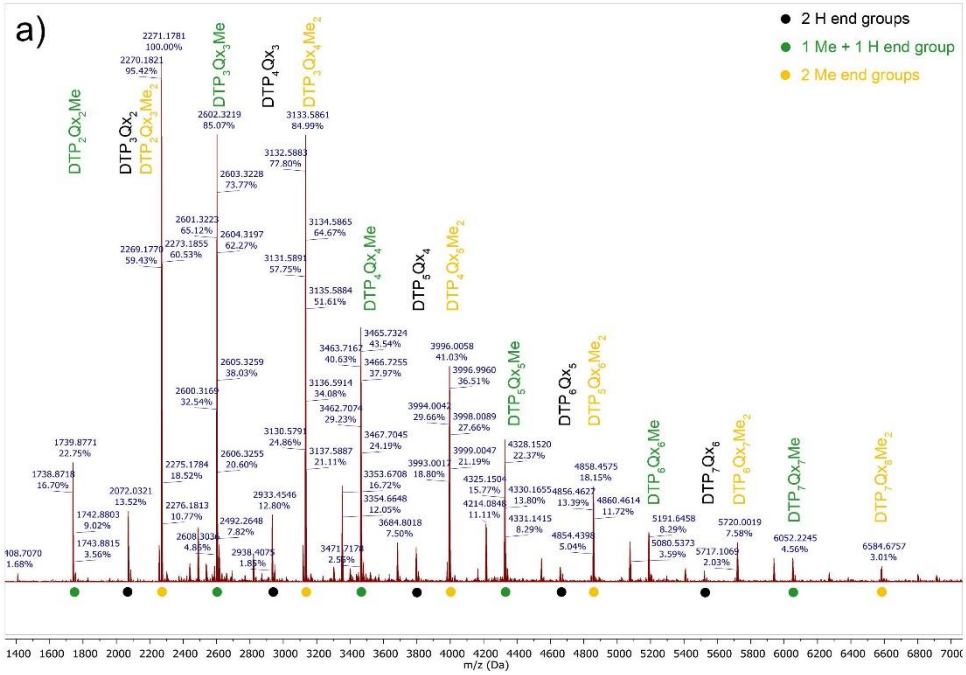
a)
2 H end groups
1 Me + 1 H end group
2 Me end groups
m/z (Da)

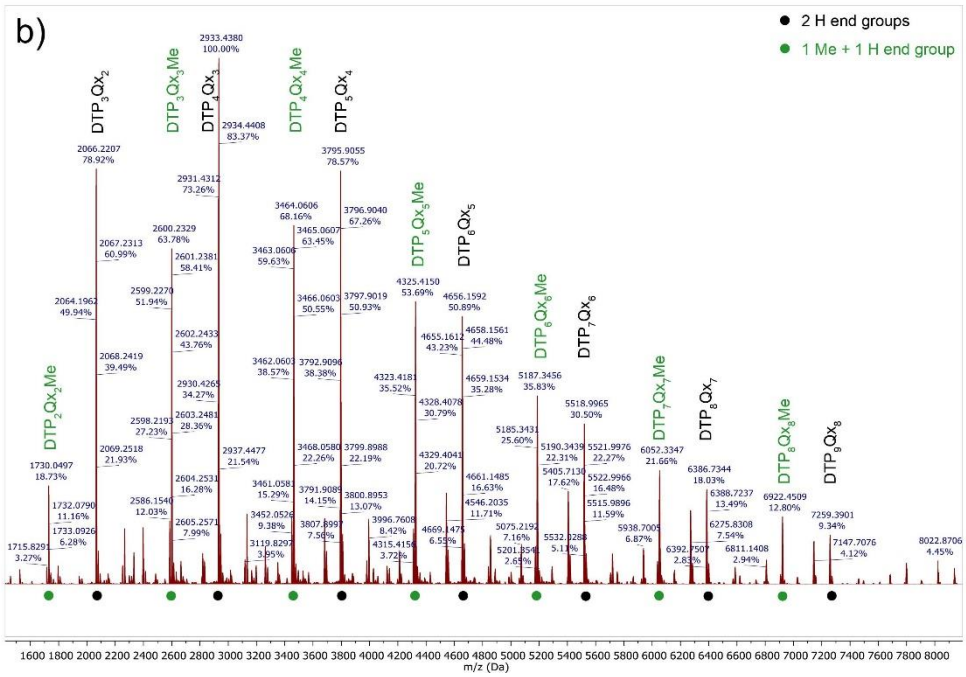
b)
2 H end groups
1 Me + 1 H end group
m/z (Da)

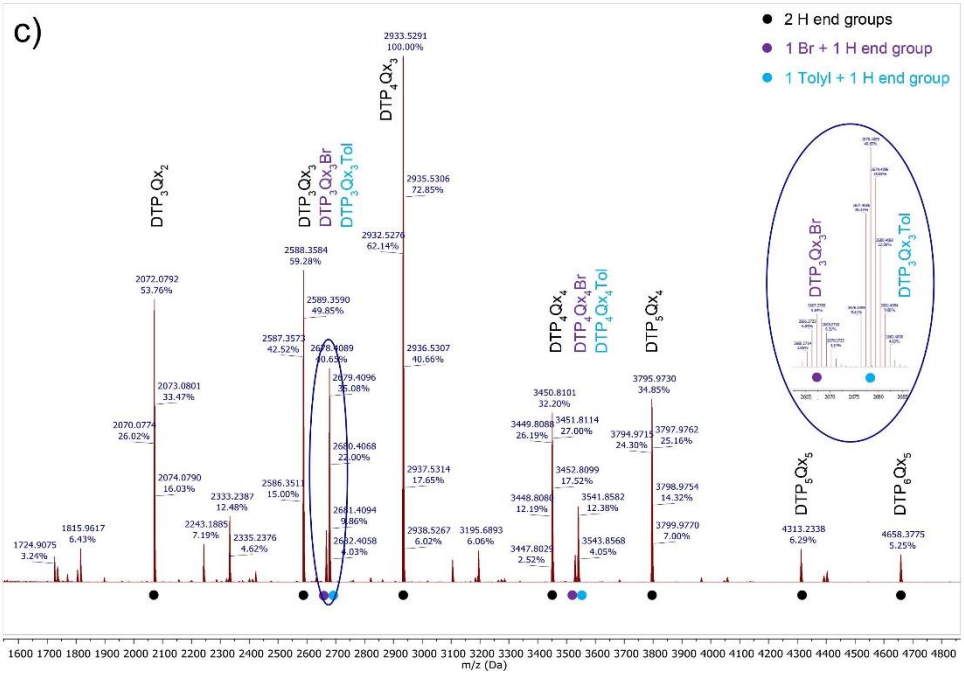

Figure 2 MALDI-ToF mass spectra of (a) the Stille-L PDTPQx polymer, (b) the Stille-H PDTPQx polymer, and (c) the DArP PDTPQx polymer (with a zoom-in of the *m/z* region from 2665 to 2685 Da).

To assess possible influences of the synthesis protocol on the materials performance in OPDs, bulk heterojunction (BHJ) blends of all polymers with $PC_{61}BM$ are analyzed in the inverted photodiode stack ITO/PEIE/PDTPQx:$PC_{61}BM$/MoO_3/Ag. Sample preparation, OPD fabrication, optimization, and characterization details can be found in the SI. First, the optimal PDTPQx:$PC_{61}BM$ ratio is determined. The 1:4 ratio affords the best results based on the dark current density (J_D) and EQE (**Figure S12**), and is therefore used in further optimizations. Second, optimization of the processing conditions for the Stille and DArP PDTPQx:$PC_{61}BM$ (1:4) blends is performed, for which the data can be found in **Figure S13-S15**. The best overall results are achieved when the active layer blend is spin-coated from chloroform with the solvent additive 1,8-diiodooctane (DIO; 5 v/v%). For all optimized devices, the current density–voltage ($J-V$) characteristics under dark (J_D) and illuminated conditions are shown in **Figure 3a**. A low J_D and a high EQE are crucial in achieving a high-efficiency photodetector with a high specific detectivity (D^*). Both Stille batches afford a significantly higher dark current than the DArP polymer in the reverse biased region, where the OPD normally operates. The difference in J_D is about two orders of magnitude at -2 V. **Figure 3b,c** shows the EQE of all optimized devices in a linear and logarithmic plot, respectively. Fourier-transform infrared (FTIR) spectroscopy is used to sensitively measure the EQE spectrum, which is plotted on a logarithmic scale in **Figure 3c**. Only for the DArP PDTPQx-based blend, a pronounced CT absorption band is present between 950 and 1150 nm. This suggests the blends differ in energetic landscape at the donor:acceptor interface, which might explain the difference in J_D and EQE. Eventually, the calculated D^* at -0.1 and -2 V is plotted in **Figure 3d** for all optimized devices (**Table S1**). Due to the high dark currents obtained with the Stille polymer batches, their EQE spectra at -2 V could not be measured as the signal is dominated by noise. Therefore, no D^* at -2 V is calculated for Stille-L and Stille-H. For the calculation of D^* at -0.1 V, both shot and thermal noise are taken into account, applying the more general equation for the specific detectivity (expressed in cm $Hz^{1/2}$ W^{-1} or Jones):

$$D^* = \frac{q\lambda EQE}{hc\sqrt{\frac{4k_B T}{R_{sh}} + 2qJ_D}} \quad (1)$$

with q the elementary charge, λ the wavelength at which the EQE is measured, h Planck's constant, c the speed of light, k_B the Boltzmann constant, and R_{sh} the shunt resistance (derived from J_D at -0.1 V). At -2 V, OPDs are shot noise limited ($4k_BT/R_{sh} << 2qJ_D$), simplifying the equation of D^*:

$$D^* = \frac{q\lambda EQE}{hc\sqrt{2qJ_D}} \quad (2)$$

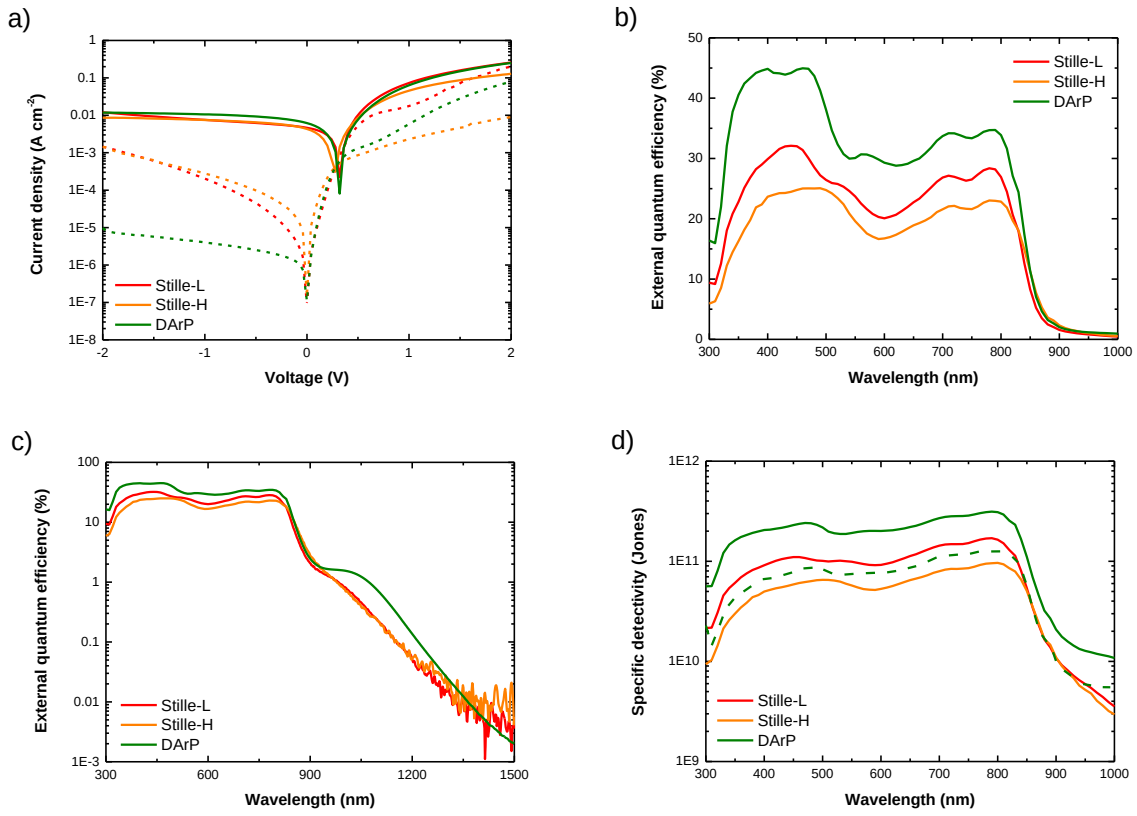

Figure 3 (a) $J-V$ curves measured under illumination (full lines) and in the dark (dashed lines) for the optimized OPD devices based on the Stille-L (red), Stille-H (orange), and DArP (green) polymer in (1:4) blends with $PC_{61}BM$. (b) EQE spectra, measured at 0 V. (c) Logarithmic plot of the sensitive EQE, measured at 0 V. (d) Calculated specific detectivities at -0.1 V (full lines) and at -2 V (dashed line).

To achieve a better understanding on the varying performance of the Stille *vs.* DArP PDTPQx, the active layer blends are investigated with atomic force microscopy (AFM). **Figure 4** shows the topography of the optimized material blends, visualizing similar surface roughness and no clear signs of extensive phase separation in any of the blends. From these images, it is clear that no large differences in surface topography exist between the optimized material blends. However, a large difference between the reference samples (processed without solvent additive) *vs.* the samples processed with DIO is observed (**Figure S16-S21**). The AFM images of the reference samples indicate some phase separation, potentially increasing J_D and decreasing the EQE, as poorly mixed donor:acceptor blends are unfavorable for photocurrent generation and might induce shunt pathways for charge carriers through the neat phases.[40]

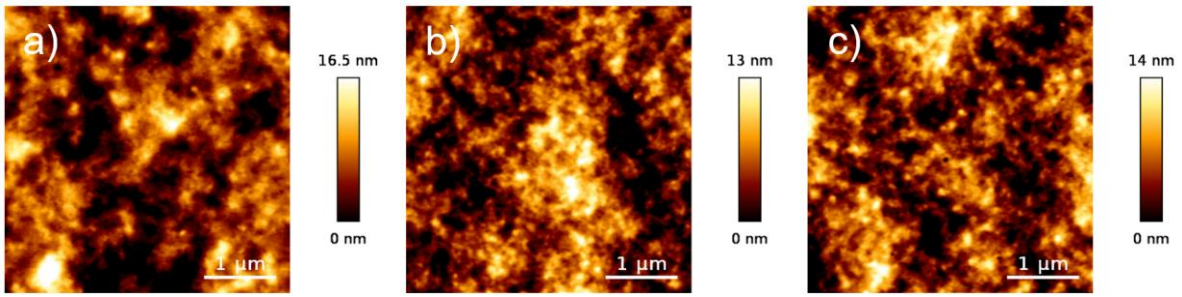

Figure 4 AFM images of optimized PDTPQx:$PC_{61}BM$ (1:4) active layers processed from chloroform with DIO (5 v/v%) based on the (a) Stille-L, (b) Stille-H, and (c) DArP polymer.

Since AFM does not clarify the extensive difference in J_D between the optimized devices, transmission electron microscopy (TEM) measurements are additionally performed (**Figure 5**). From these measurements, it is clear that all material blends are amorphous (diffraction patterns are shown in **Figure S22-S27**). A small difference in morphology can be observed between the Stille-L active layer on the one hand, and the Stille-H and DArP active layers on the other hand, as somewhat larger domains exist in the Stille-L blend. This distinction probably originates from the molar mass variation of the polymers. No apparent differences in morphology between the Stille-H and DArP blends are observed. Similar to the AFM measurements, a significant difference between the reference samples *vs.* the samples processed with DIO is seen (**Figure S22-S27**), again stressing the morphological benefit of the use of solvent additives. However, the differences in J_D and EQE can not be explained based on these microscopy results. Additional photoluminescence quenching experiments did not indicate any noticeable difference between the blends either (**Figure S28**).

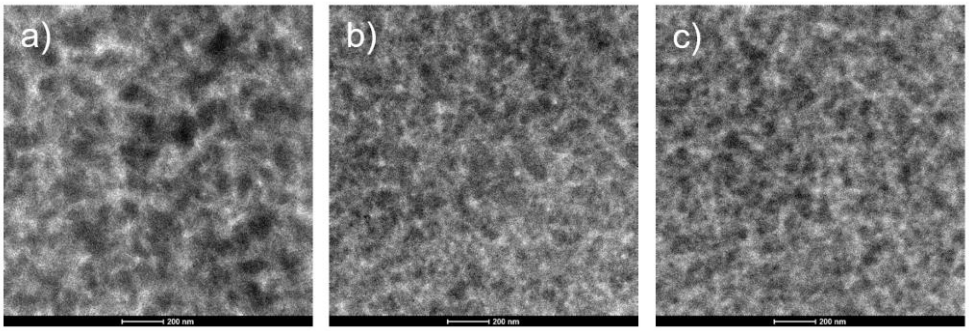

Figure 5 TEM images of optimized PDTPQx:$PC_{61}BM$ (1:4) active layers processed from chloroform with DIO (5 v/v%) based on the (a) Stille-L, (b) Stille-H, and (c) DArP polymer batch.

Because of the distinct CT band observed in the 950 to 1150 nm region for the DArP PDTPQx:$PC_{61}BM$ (1:4) blend (**Figure 3c**), a resonant optical cavity photodetector is fabricated for this blend. This particular type of photodetector lends itself to wavelength selective photodetection at the tunable resonance wavelengths.[6, 23] For a Fabry-Pérot cavity, the resonance wavelength is proportional to both the cavity thickness and the effective refractive index of the photoactive layer.[41,42] The cavity device stack consists of the DArP PDTPQx:$PC_{61}BM$ (1:4) active layer blend processed from chloroform with solvent additive DIO (5 v/v%), with PEIE as electron transport layer and MoO_3 as hole transport layer, sandwiched between a thick non-transparent and a thin semi-transparent Ag electrode on a glass substrate. All details about the cavity OPD fabrication can be found in the SI. For the devices with a 180 nm and a 210 nm thick BHJ active layer (**Figure 6**), EQEs of 2.5% at 1016 nm and 1% at 1140 nm are achieved with rather narrow peak responses with a full-width-at-half-maximum (FWHM) of 44 and 45 nm, respectively, and specific detectivities of 2.24 x 10^{10} and 1.06 x 10^{10} Jones (calculated at -0.1 V) (**Table S2**). For all PDTPQx:$PC_{61}BM$ (1:4) based devices, an undulating surface was observed when

monitoring the blend thickness with a profilometer. Future optimization of the blend surface morphology and homogeneity of the blend thickness, directly linked to the EQE and FWHM in an optical cavity OPD,[25] could possibly further enhance the detectivities.

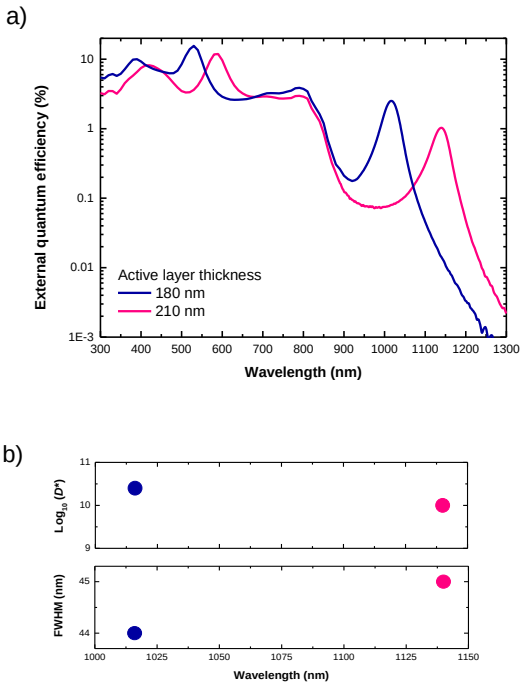

Figure 6 (a) EQEs of the optical resonant cavity OPD based on the DArP PDTPQx:$PC_{61}BM$ (1:4) blend, with active layer thicknesses of 180 nm (in blue) and 210 nm (in pink). (b) Calculated detectivities (at -0.1 V) and FWHM values of the resonance peaks between 1000 and 1150 nm.

3. Conclusions

The high-HOMO polymer PDTPQx is synthesized *via* both Stille polycondensation and (the more sustainable alternative) direct arylation polymerization, yielding three polymers named Stille-L, Stille-H, and DArP. Near-infrared organic photodetectors are constructed based on these different polymer batches, and their performances are investigated. The ITO/PEIE/PDTPQx:$PC_{61}BM$(1:4)/MoO_3/Ag device stack, with the active layer blend processed from chloroform with solvent additive DIO (5 v/v%), shows the best overall results. From the $J-V$ characteristics it is clear that the DArP-based devices outperform the Stille-based devices. Only the DArP-based device shows a clear charge-transfer absorption band in the sensitively measured EQE spectrum. Furthermore, specific detectivities at -2 V are calculated, only for the DArP-based device, as the dark current of the Stille-based devices is too high and dominated by noise. Because of the distinct charge-transfer absorption band of the DArP-based device, optical resonant cavity OPDs are made for that specific material blend. Those devices show peak EQEs of 2.5% and 1% at resonance wavelengths of 1016 and 1140 nm, with full-width-at-half-maximum peak responses of 44 and 45 nm and detectivities of 2.24 x 10^{10} and 1.06 x 10^{10} Jones, respectively. The origin of the performance gap between the devices based on the Stille polymers on the one hand, and the DArP polymer on the other hand, remains unknown for now. AFM and TEM measurements indicate no substantial differences in topography and bulk morphology, respectively. Comparing Stille-H and DArP, the similar melting enthalpy also indicates a similar degree of crystallinity. Whereas the high-temperature NMR spectra of the highest molar mass Stille and the DArP polymer are very similar, MALDI-ToF mass spectrometry reveals that the main difference between the different polymers is in the end groups, which are not expected to play such a crucial role. In any case,

this once again illustrates that there is still much to learn on the effect of subtle structural variations of push-pull conjugated polymers on their performance in organic electronic devices, and further efforts in this direction are certainly required.[19, 20]

Acknowledgements

The authors thank Huguette Penxten for CV analysis, Christel Willems for the TEM sample preparation, and Brent Fripont for the graphical abstract artwork. We also thank the Research Foundation – Flanders (FWO Vlaanderen) for continuing financial support (projects G0D0118N, G0B2718N, 1S50820N, 11D2618N), as well as the European Research Council (ERC, grant agreement 864625). Dr. Q. Liu acknowledges financial support from the European Union's Horizon 2020 research and innovation program under the Marie-Curie grant agreement no. 88279.

References

1. Ostroverkhova, O., Organic Optoelectronic Materials: Mechanisms and Applications. *Chemical Reviews* **2016,** *116*, 13279-13412.
2. Pankow, R. M.; Thompson, B. C., The development of conjugated polymers as the cornerstone of organic electronics. *Polymer* **2020,** *207*, 122874.
3. Wang, T.; Kupgan, G.; Brédas, J.-L., Organic Photovoltaics: Relating Chemical Structure, Local Morphology, and Electronic Properties. *Trends in Chemistry* **2020,** *2*, 535-554.
4. Pode, R., Organic light emitting diode devices: An energy efficient solid state lighting for applications. *Renewable and Sustainable Energy Reviews* **2020,** *133*, 110043.
5. Ren, H.; Chen, J.-D.; Li, Y.-Q.; Tang, J.-X., Recent Progress in Organic Photodetectors and their Applications. *Advanced Science* **2021,** *8*, 2002418.
6. Vanderspikken, J.; Maes, W.; Vandewal, K., Wavelength-Selective Organic Photodetectors. *Advanced Functional Materials* **2021,** *31*, 2104060.
7. Kim, M.; Ryu, S. U.; Park, S. A.; Choi, K.; Kim, T.; Chung, D.; Park, T., Donor–Acceptor-Conjugated Polymer for High-Performance Organic Field-Effect Transistors: A Progress Report. *Advanced Functional Materials* **2020,** *30*, 1904545.
8. Rivnay, J.; Inal, S.; Salleo, A.; Owens, R. M.; Berggren, M.; Malliaras, G. G., Organic electrochemical transistors. *Nature Reviews Materials* **2018,** *3*, 17086.
9. Bronstein, H.; Nielsen, C. B.; Schroeder, B. C.; McCulloch, I., The role of chemical design in the performance of organic semiconductors. *Nature Reviews Chemistry* **2020,** *4*, 66-77.
10. Carsten, B.; He, F.; Son, H. J.; Xu, T.; Yu, L., Stille Polycondensation for Synthesis of Functional Materials. *Chemical Reviews* **2011,** *111*, 1493-1528.
11. Sakamoto, J.; Rehahn, M.; Wegner, G.; Schlüter, A. D., Suzuki Polycondensation: Polyarylenes à la Carte. *Macromolecular Rapid Communications* **2009,** *30*, 653-687.
12. Osaka, I.; McCullough, R. D., Advances in Molecular Design and Synthesis of Regioregular Polythiophenes. *Accounts of Chemical Research* **2008,** *41*, 1202-1214.
13. Chen, T.-A.; Wu, X.; Rieke, R. D., Regiocontrolled Synthesis of Poly(3-alkylthiophenes) Mediated by Rieke Zinc: Their Characterization and Solid-State Properties. *Journal of the American Chemical Society* **1995,** *117*, 233-244.
14. Alberico, D.; Scott, M. E.; Lautens, M., Aryl−Aryl Bond Formation by Transition-Metal-Catalyzed Direct Arylation. *Chemical Reviews* **2007,** *107*, 174-238.
15. Gobalasingham, N. S.; Thompson, B. C., Direct arylation polymerization: A guide to optimal conditions for effective conjugated polymers. *Progress in Polymer Science* **2018,** *83*, 135-201.
16. Di Mauro, E.; Rho, D.; Santato, C., Biodegradation of bio-sourced and synthetic organic electronic materials towards green organic electronics. *Nature Communications* **2021,** *12*, 3167.
17. Tropp, J.; Rivnay, J., Design of biodegradable and biocompatible conjugated polymers for bioelectronics. *Journal of Materials Chemistry C* **2021,** *9*, 13543.

18. Ponder Jr, J. F.; Chen, H.; Luci, A. M. T.; Moro, S.; Turano, M.; Hobson, A. L.; Collier, G. S.; Perdigão, L. M. A.; Moser, M.; Zhang, W.; Costantini, G.; Reynolds, J. R.; McCulloch, I., Low-Defect, High Molecular Weight Indacenodithiophene (IDT) Polymers Via a C–H Activation: Evaluation of a Simpler and Greener Approach to Organic Electronic Materials. *ACS Materials Letters* **2021**, 1503-1512.
19. Qiu, Z.; Hammer, B. A. G.; Müllen, K., Conjugated polymers – Problems and promises. *Progress in Polymer Science* **2020,** *100*, 101179.
20. Pirotte, G.; Verstappen, P.; Vanderzande, D.; Maes, W., On the "True" Structure of Push–Pull-Type Low-Bandgap Polymers for Organic Electronics. *Advanced Electronic Materials* **2018,** *4*, 1700481.
21. Vangerven, T.; Verstappen, P.; Drijkoningen, J.; Dierckx, W.; Himmelberger, S.; Salleo, A.; Vanderzande, D.; Maes, W.; Manca, J. V., Molar Mass versus Polymer Solar Cell Performance: Highlighting the Role of Homocouplings. *Chemistry of Materials* **2015,** *27*, 3726-3732.
22. Siegmund, B.; Mischok, A.; Benduhn, J.; Zeika, O.; Ullbrich, S.; Nehm, F.; Böhm, M.; Spoltore, D.; Fröb, H.; Körner, C.; Leo, K.; Vandewal, K., Organic narrowband near-infrared photodetectors based on intermolecular charge-transfer absorption. *Nature Communications* **2017,** *8*, 15421.
23. Tang, Z.; Ma, Z.; Sánchez-Díaz, A.; Ullbrich, S.; Liu, Y.; Siegmund, B.; Mischok, A.; Leo, K.; Campoy-Quiles, M.; Li, W.; Vandewal, K., Polymer:Fullerene Bimolecular Crystals for Near-Infrared Spectroscopic Photodetectors. *Advanced Materials* **2017,** *29*, 1702184.
24. Kaiser, C.; Schellhammer, K. S.; Benduhn, J.; Siegmund, B.; Tropiano, M.; Kublitski, J.; Spoltore, D.; Panhans, M.; Zeika, O.; Ortmann, F.; Meredith, P.; Armin, A.; Vandewal, K., Manipulating the Charge Transfer Absorption for Narrowband Light Detection in the Near-Infrared. *Chemistry of Materials* **2019,** *31*, 9325-9330.
25. Vanderspikken, J.; Liu, Q.; Liu, Z.; Vandermeeren, T.; Cardeynaels, T.; Gielen, S.; Van Mele, B.; Van den Brande, N.; Champagne, B.; Vandewal, K.; Maes, W., Tuning Electronic and Morphological Properties for High-Performance Wavelength-Selective Organic Near-Infrared Cavity Photodetectors. *Advanced Functional Materials* **2021**, *31*, 2108146.
26. Rasmussen, S. C.; Evenson, S. J., Dithieno[3,2-b:2',3'-d]pyrrole-based materials: Synthesis and application to organic electronics. *Progress in Polymer Science* **2013,** *38*, 1773-1804.
27. Geng, Y.; Tang, A.; Tajima, K.; Zeng, Q.; Zhou, E., Conjugated materials containing dithieno[3,2-b:2',3'-d]pyrrole and its derivatives for organic and hybrid solar cell applications. *Journal of Materials Chemistry A* **2019,** *7*, 64-96.
28. Vanormelingen, W.; Kesters, J.; Verstappen, P.; Drijkoningen, J.; Kudrjasova, J.; Koudjina, S.; Liégeois, V.; Champagne, B.; Manca, J.; Lutsen, L.; Vanderzande, D.; Maes, W., Enhanced open-circuit voltage in polymer solar cells by dithieno[3,2-b:2',3'-d]pyrrole N-acylation. *Journal of Materials Chemistry A* **2014,** *2*, 7535-7545.
29. Kesters, J.; Verstappen, P.; Vanormelingen, W.; Drijkoningen, J.; Vangerven, T.; Devisscher, D.; Marin, L.; Champagne, B.; Manca, J.; Lutsen, L.; Vanderzande, D.; Maes, W., N-acyl-dithieno[3,2-b:2',3'-d]pyrrole-based low bandgap copolymers affording improved open-circuit voltages and efficiencies in polymer solar cells. *Solar Energy Materials and Solar Cells* **2015,** *136*, 70-77.
30. Raymakers, J.; Haenen, K.; Maes, W., Diamond surface functionalization: from gemstone to photoelectrochemical applications. *Journal of Materials Chemistry C* **2019,** *7*, 10134-10165.
31. Gedefaw, D.; Prosa, M.; Bolognesi, M.; Seri, M.; Andersson, M. R., Recent Development of Quinoxaline Based Polymers/Small Molecules for Organic Photovoltaics. *Advanced Energy Materials* **2017,** *7*, 1700575.
32. Yang, J.; Cong, P.; Chen, L.; Wang, X.; Li, J.; Tang, A.; Zhang, B.; Geng, Y.; Zhou, E., Introducing Fluorine and Sulfur Atoms into Quinoxaline-Based p-type Polymers to Gradually Improve the Performance of Fullerene-Free Organic Solar Cells. *ACS Macro Letters* **2019,** *8*, 743-748.
33. Xiao, B.; Zhang, Q.; Li, G.; Du, M.; Geng, Y.; Sun, X.; Tang, A.; Liu, Y.; Guo, Q.; Zhou, E., Side chain engineering of quinoxaline-based small molecular nonfullerene acceptors for high-performance poly(3-hexylthiophene)-based organic solar cells. *Science China Chemistry* **2020,** *63*, 254-264.
34. Mishra, S. P.; Palai, A. K.; Srivastava, R.; Kamalasanan, M. N.; Patri, M., Dithieno[3,2-b:2',3'-d]pyrrole–alkylthiophene–benzo[c][1,2,5]thiadiazole-based highly stable and low band gap polymers

for polymer light-emitting diodes. *Journal of Polymer Science Part A: Polymer Chemistry* **2009,** *47*, 6514-6525.
35. Marin, L.; Lutsen, L.; Vanderzande, D.; Maes, W., Quinoxaline derivatives with broadened absorption patterns. *Organic & Biomolecular Chemistry* **2013,** *11*, 5866-5876.
36. Wakioka, M.; Torii, N.; Saito, M.; Osaka, I.; Ozawa, F., Donor–Acceptor Polymers Containing 4,8-Dithienylbenzo[1,2-b:4,5-b′]dithiophene via Highly Selective Direct Arylation Polymerization. *ACS Applied Polymer Materials* **2021,** *3*, 830-836.
37. Tong, M.; Cho, S.; Rogers, J. T.; Schmidt, K.; Hsu, B. B. Y.; Moses, D.; Coffin, R. C.; Kramer, E. J.; Bazan, G. C.; Heeger, A. J., Higher Molecular Weight Leads to Improved Photoresponsivity, Charge Transport and Interfacial Ordering in a Narrow Bandgap Semiconducting Polymer. *Advanced Functional Materials* **2010,** *20*, 3959-3965.
38. Spoltore, D.; Vangerven, T.; Verstappen, P.; Piersimoni, F.; Bertho, S.; Vandewal, K.; Van den Brande, N.; Defour, M.; Van Mele, B.; De Sio, A.; Parisi, J.; Lutsen, L.; Vanderzande, D.; Maes, W.; Manca, J. V., Effect of molecular weight on morphology and photovoltaic properties in P3HT:PCBM solar cells. *Organic Electronics* **2015,** *21*, 160-170.
39. Liu, Q.; Smeets, S.; Mertens, S.; Xia, Y.; Maes, W.; Vandewal, K., Narrow electroluminescence linewidths for reduced non-radiative recombination in organic photovoltaics and near-infrared light-emitting diodes. *Joule* **2021,** *5*, 2365-2379.
40. Verstraeten, F.; Gielen, S.; Verstappen, P.; Kesters, J.; Georgitzikis, E.; Raymakers, J.; Cheyns, D.; Malinowski, P.; Daenen, M.; Lutsen, L.; Vandewal, K.; Maes, W., Near-infrared organic photodetectors based on bay-annulated indigo showing broadband absorption and high detectivities up to 1.1 µm. *Journal of Materials Chemistry C* **2018,** *6*, 11645-11650.
41. Ünlü, M. S.; Strite, S., Resonant cavity enhanced photonic devices. *Journal of Applied Physics* **1995,** *78*, 607-639.
42. Liu, Q.; Toudert, J.; Li, T.; Kramarenko, M.; Martínez-Denegri, G.; Ciammaruchi, L.; Zhan, X.; Martorell, J., Inverse Optical Cavity Design for Ultrabroadband Light Absorption Beyond the Conventional Limit in Low-Bandgap Nonfullerene Acceptor–Based Solar Cells. *Advanced Energy Materials* **2019,** *9*, 1900463.

Supporting Information

A PDTPQx:$PC_{61}BM$ Blend with Pronounced Charge-Transfer Absorption for Organic Resonant Cavity Photodetectors – Direct Arylation Polymerization vs. Stille Polycondensation

*Tom Vandermeeren[a,b,c], Quan Liu[a,b,c], Sam Gielen[a,b,c], Dries Theunissen[a,b,c], Siebe Frederix[a,b,c], Melissa Van Landeghem[a,b,c], Zhen Liu[d], Niko Van den Brande[d], Jan D'Haen[a,b,c], Jochen Vanderspikken[a,b,c], Laurence Lutsen[a,b,c], Koen Vandewal[a,b,c], Wouter Maes[a,b,c]**

[a] Hasselt University, Institute for Materials Research (IMO), Agoralaan Building D, 3590 Diepenbeek, Belgium
[b] IMEC, Associated Lab IMOMEC, Wetenschapspark 1, 3590 Diepenbeek, Belgium
[c] Energyville, Thorpark, 3600 Genk, Belgium
[d] Vrije Universiteit Brussel, Physical Chemistry and Polymer Science, Pleinlaan 2, 1050 Brussels, Belgium

* *Corresponding author. E-mail address: wouter.maes@uhasselt.be*

Table of contents

1. Materials and methods

Preparative (recycling) size exclusion chromatography (prep-SEC) was performed on a JAI LC-9110 NEXT system equipped with JAIGEL 1H and 2H columns (eluent $CHCl_3$, flow rate 3.5 mL min^{-1}). NMR chemical shifts (δ, in ppm) of all precursors and monomers were determined relative to the residual $CHCl_3$ (7.26 ppm, singlet) signal or the ^{13}C resonance shift of $CDCl_3$ (77.16 ppm, triplet) at room temperature. NMR chemical shifts (δ, in ppm) of the polymers were determined relative to the residual 1,2-dichlorobenzene (6.93 ppm, singlet; 7.19 ppm, singlet) signals at 110 °C. Polymer molar mass distributions were estimated by size exclusion chromatography at 160 °C on an Agilent 1260 Infinity II High-Temperature GPC (HT-GPC) system using a PL-GEL 10 µm MIXED-B column with 1,2,4-trichlorobenzene as the eluent and using polystyrene internal standards. Matrix-assisted laser desorption/ionization - time-of-flight (MALDI-ToF) mass spectra were recorded on a Bruker UltrafleXtreme™ MALDI-TOF/TOF system. Approximately 10 µL of the matrix solution (25 mg mL^{-1} *trans*-2-[3-(4-*tert*-butylphenyl)-2-methyl-2-propenylidene]malononitrile (DTCB) in chloroform) was mixed with 3 µL of the analyte solution (10 mg mL^{-1} in chloroform), after which 0.5 µL of the resulting solution was spotted onto an MTP Anchorchip 600/384 MALDI plate. Background corrected UV-Vis-NIR absorption spectroscopy measurements were performed on a VARIAN Cary 5000 UV-Vis-NIR spectrophotometer at a scan rate of 600 nm min^{-1}. The films for the UV-Vis-NIR absorption measurements were prepared either by drop-casting a solution of the respective polymer in $CHCl_3$ on a quartz substrate (for the data presented in Figure 1) or by spin-coating on a glass substrate (for the data presented in Figure S9). Absorption coefficients were determined using the DRA 2500 internal diffuse reflectance accessory. By measuring both the transmission (T) and reflectance (R), the absorption coefficient was calculated as $\alpha = -1/d\ ln(T/(100\% - R))$, hereby neglecting weak interference effects. Three different film thicknesses were used for all polymers and average values were determined. The solid-state UV-Vis-NIR absorption spectra were used to estimate the optical gaps (from the wavelength at the intersection of the tangent line drawn at the low energy side of the absorption spectrum with the baseline: $E_g\ (eV) = 1240/(wavelength\ in\ nm)$). Electrochemical measurements (cyclic voltammetry, CV) were performed with an Eco Chemie Autolab PGSTAT 30 potentiostat/galvanostat using a three-electrode microcell with a platinum working electrode, a platinum counter electrode, and a $Ag/AgNO_3$ reference electrode (silver wire dipped in a solution of 0.01 M $AgNO_3$ and 0.1 M NBu_4PF_6 in anhydrous acetonitrile). The reference electrode was calibrated against ferrocene/ferrocenium as external standard. Sample preparation was done by dip-coating the platinum working electrode in the respective polymer solutions. The CV measurements were done on the resulting films with 0.1 M NBu_4PF_6 in anhydrous acetonitrile as electrolyte solution. The experiments were carried out under a curtain of argon to prevent air from entering the system. Cyclic voltammograms were recorded at a scan rate of 100 mV s^{-1}. For the conversion of V to eV, the onset potentials of the first oxidation/reduction peaks were used and referenced to ferrocene/ferrocenium, which has an ionization potential of −4.98 eV *vs.* vacuum. This correction factor is based on a value of 0.31 eV for Fc/Fc^+ *vs*. SCE[1] and a value of 4.68 eV for SCE *vs.* vacuum[2]: $E_{\mathrm{HOMO/LUMO}}\ (eV) = -4.98 - E^{\mathrm{Ag/AgNO_3}}_{\mathrm{onset\ ox/red}}\ (V) + E^{\mathrm{Ag/AgNO_3}}_{\mathrm{onset\ Fc/Fc^+}}(V)$. The accuracy of measuring redox potentials by CV is about 0.01–0.02 V. Reproducibility issues can occur due to the dependence of the potentials on concentration and temperature. Thermogravimetric analysis (TGA) was performed on a TA Instruments TGA Q5000. Measurements were performed at a heating rate of 20 K min^{-1} using nitrogen (25 mL min^{-1}) as the purge gas. Sample masses of approximately 1 mg were used. Rapid heat-cool calorimetry (RHC) was performed using a protype instrument from TA Instruments. Experiments were performed at a heating rate of 500 K min^{-1} and a cooling rate of 20 K min^{-1}, with nitrogen (6 mL min^{-1}) as the purge gas. Dedicated aluminum RHC crucibles were filled with around 200–250 µg of the

respective polymer sample. A first heating was used to remove the thermal history and therefore all thermograms shown correspond to the second heating. Photoluminescence (PL) experiments were performed at room temperature under excitation with a 405 nm pulsed diode laser (Thorlabs, NPL41C, 6 ns pulse length and 4.1 nJ per pulse). Backscattered PL emission was diffracted in a grating spectrograph (Andor, Kymera 328i-D2-SIL) and registered by a linear CCD detector (Andor, iDus 416-LDC-DD). Unwanted laser reflections were eliminated from the spectrum by means of a 405 nm notch filter in front of the spectrograph entrance. To avoid photodegradation, the devices were mounted in N_2 atmosphere in an airtight sample holder. All spectra were corrected for the spectral response of the set-up determined using a calibrated light source (Avantes, AvaLight-HAL-CAL-Mini).

2. Materials synthesis and characterization

All reagents and chemicals were obtained from commercial sources and used without further purification. Solvents were dried by a solvent purification system (MBraun, MB-SPS-800) equipped with alumina columns. All moisture-sensitive reactions were carried out under inert atmosphere and in flame-dried glassware. Reactions were magnetically stirred and monitored by TLC (pre-coated silica gel, 60 Å average pore diameter, 254 µm, aluminum foil supported TLC plates). Compounds were visualized by UV S4 irradiation (254 nm). Automatic column chromatography was performed using a Buchi SepacoreTM flash apparatus, consisting of a C-660 Buchi fraction collector, C-615 Pump manager, C-630 UV Monitor, and two C-601 pump modules. Solvents were evaporated with a rotavapor at a temperature of 45 °C. Yields refer to isolated compounds.

4-Dodecyl-4*H*-dithieno[3,2-*b*:2',3'-*d*]pyrrole (2). 3,3'-Dibromo-2,2'-bithiophene (0.65 g, 2 mmol), dodecylamine (0.74 g, 4 mmol), tris(dibenzylideneacetone)dipalladium(0) (92 mg, 0.1 mmol), BINAP (0.25 g, 0.4 mmol), and sodium *tert*-butoxide (0.48 g, 5 mmol) were dissolved in 20 mL of dry and degassed toluene under inert atmosphere. The reaction mixture was purged with N_2 gas for 30 min, after which it was stirred at 120 °C for 19 h. The reaction was quenched with water, extracted with diethyl ether (3 x 10 mL), and then extracted with DCM (3 x 10 mL). The combined organic layers were dried over anhydrous Na_2SO_4. After filtration of the drying agent and removing the solvent under reduced pressure, the crude product was further purified by column chromatography (silica gel; petroleum ether:DCM, 93:7). Compound **2** (0.58 g, 84%) was obtained as a yellowish oil. ^{1}H NMR ($CDCl_3$, 400 MHz, ppm): 7.12 (d, *J* = 5.3 Hz, 2H), 6.99 (d, *J* = 5.3 Hz, 2H), 4.18 (t, *J* = 7.1 Hz, 2H), 1.85 (p, *J* = 7.2 Hz, 2H), 1.31 – 1.20 (m, 18H), 0.87 (t, *J* = 7.0 Hz, 3H). ^{13}C NMR ($CDCl_3$, 100 MHz, ppm): 145.6, 123.4, 115.3, 111.6, 48.1, 32.59, 31.1, 30.3, 30.3, 30.2, 30.1, 30.0, 29.9, 27.7, 23.4, 14.8. Analytical data were in accordance with data previously reported in the literature.[3]

4-Dodecyl-2,6-bis(trimethylstannyl)-4*H*-dithieno[3,2-*b*:2',3'-*d*]pyrrole (3). 4-Dodecyl-4*H*-dithieno-[3,2-*b*:2',3'-*d*]pyrrole (2.09 g, 6 mmol) was dissolved in 60 mL of dry and degassed THF and the solution was stirred at -78 °C. A *n*-butyllithium solution (5.8 mL, 14.4 mmol) was added dropwise while stirring. After stirring for 1 h while slowly warming up the reaction mixture to RT, a trimethyltin chloride solution (14.4 mL, 14.4 mmol) was added dropwise at -78 °C. The reaction mixture was left to warm up to ambient temperature and stirred for 24 h. The reaction mixture was quenched with water and extracted with diethyl ether (3 x 30 mL). The combined ether layers were washed with brine once and then dried over anhydrous $MgSO_4$. After filtration of the drying agent and removing the solvent under reduced pressure, the crude product was further purified by prep-SEC. Compound **3** was obtained as a dark green oil (2.61 g, 65%). ^{1}H NMR ($CDCl_3$, 400 MHz): δ (ppm) = 6.99 (s, 2H), 4.16 (t, *J* = 7.1 Hz, 2H), 1.86 (p, *J* = 7.2 Hz, 2H), 1.32 – 1.21 (m, 18H), 0.87 (t, *J* = 7.0 Hz, 3H), 0.39 (s, 18H). ^{13}C NMR ($CDCl_3$, 100

MHz): δ (ppm) = 148.0, 135.7, 120.3, 118.0, 47.5, 32.0, 30.6, 29.8, 29.8, 29.8, 29.7, 29.5, 29.4, 27.1, 22.8, 14.3, -8.0. Analytical data were in accordance with data previously reported in the literature.[3]

2-(2-Ethylhexyl)thiophene (5). Thiophene (11 mL, 140 mmol) was dissolved in 70 mL of dry and degassed THF and the solution was stirred at -78 °C. A *n*-butyllithium solution (56 mL, 140 mmol) was added dropwise and the resulting mixture was stirred for 1 h at -78 °C, after which KI (1.16 g, 7 mmol) was added and the mixture was purged with N_2. Next, 2-ethylhexyl bromide (30 mL, 168 mmol) was added dropwise. The reaction mixture was left to warm up to ambient temperature and stirred for 18 h. The reaction mixture was quenched by pouring it into water and extracted with diethyl ether (3 x 75 mL). The combined organic layers were washed with brine and dried over anhydrous $MgSO_4$. After filtration of the drying agent and removing the solvent under reduced pressure, the crude product was further purified by column chromatography (silica gel; petroleum ether). Compound **5** was obtained as a colorless oil (5.35 g, 20%). ^{1}H NMR ($CDCl_3$, 400 MHz): δ (ppm) = 7.10 (dd, *J* = 5.1, 1.2 Hz, 1H), 6.90 (dd, *J* = 5.1, 3.4 Hz, 1H), 6.78 – 6.72 (m, 1H), 2.75 (d, *J* = 6.8 Hz, 2H), 1.62 – 1.49 (m, 1H), 1.34 – 1.20 (m, 8H), 0.94 – 0.80 (m, 6H). Analytical data were in accordance with data previously reported in the literature.[4]

1,2-Bis(5-(2-ethylhexyl)thiophen-2-yl)ethane-1,2-dione (6). $AlCl_3$ (7.56 g, 56.7 mmol) was dissolved in 30 mL of dry and degassed dichloromethane (DCM) and the mixture was stirred at -20 °C. Oxalyl chloride (1.14 mL, 13.5 mmol) was dissolved in 10 mL of dry and degassed DCM and added to the cooled $AlCl_3$ solution. 2-(2-Ethylhexyl)thiophene (5.30 g, 27 mmol) and pyridine (2 mL, 24.3 mmol) were dissolved in 15 mL of dry and degassed DCM and were added dropwise to the $AlCl_3$/oxalyl chloride mixture, while stirring at -20 °C. The reaction mixture was left to heat up to ambient temperature and stirred for 20 h. The reaction mixture was poured out in ice water, extracted with DCM (3 x 40 mL), and dried over anhydrous $MgSO_4$. After filtration of the drying agent and removing the solvent under reduced pressure, the crude product was further purified by column chromatography (silica, petroleum ether:ethyl acetate, 95:5). Compound **6** was obtained as an orange oil (2.94 g, 24%). ^{1}H NMR ($CDCl_3$, 400 MHz): δ (ppm) = 7.86 (d, *J* = 3.9 Hz, 2H), 6.85 (d, *J* = 3.9 Hz, 2H), 2.81 (d, *J* = 6.9 Hz, 4H), 1.67 – 1.59 (m, 2H), 1.39 – 1.19 (m, 16H), 0.92 – 0.83 (m, 12H). Analytical data were in accordance with data previously reported in the literature.[4]

3,6-Dibromobenzene-1,2-diamine (8). 4,7-Dibromobenzo[*c*][1,2,5]thiadiazole (5.00 g, 17 mmol) was dissolved in 20 mL of ethanol. $NaBH_4$ (9.65 g, 255 mmol) was added in small portions and the reaction mixture was stirred at RT for 27 h. The reaction mixture was quenched with water, extracted with ethyl acetate (3 x 20 mL), and the combined organic layers were dried over anhydrous $MgSO_4$. After filtration of the drying agent and removing the solvent under reduced pressure, the crude product was further purified by column chromatography (silica gel; petroleum ether:ethyl acetate, 85:15). Compound **8** was obtained as a slightly yellow solid (2.31 g, 51%). ^{1}H NMR ($CDCl_3$, 400 MHz): δ (ppm) = 6.84 (s, 2H), 3.89 (s, 4H). Analytical data were in accordance with data previously reported in the literature.[5]

5,8-Dibromo-2,3-bis(5-(2-ethylhexyl)thiophen-2-yl)quinoxaline (9). 3,6-Dibromobenzene-1,2-diamine (1.75 g, 6.6 mmol), 1,2-bis(5-(2-ethylhexyl)thiophen-2-yl)ethane-1,2-dione (2.94 g, 6.6 mmol) and *para*-toluenesulfonic acid monohydrate (0.13 g, 0.66 mmol) were dissolved in 120 mL of methanol and the mixture was stirred at 70 °C for 16 h. The reaction mixture was then cooled to 0 °C and the formed precipitate was isolated by filtration and washed with cold MeOH. Compound **9** was obtained as a yellow solid (3.28 g, 73%). ^{1}H NMR ($CDCl_3$, 400 MHz): δ (ppm) = 7.75 (s, 2H), 7.37 (d, *J* = 3.7 Hz, 2H), 6.67 (d, *J* = 3.7 Hz, 2H), 2.79 (d, *J* = 6.8 Hz, 4H), 1.64 (p, *J* = 6.0 Hz, 2H), 1.42 – 1.23 (m, 16H), 0.89 (t, *J* = 7.4 Hz, 12H). ^{13}C NMR ($CDCl_3$, 100 MHz): δ (ppm) = 151.5, 147.9, 139.2, 139.1, 133.3, 131.0, 126.7,

123.6, 42.1, 35.2, 33.1, 29.5, 26.3, 23.7, 14.9, 11.5. Analytical data were in accordance with data previously reported in the literature.[4]

Poly{[4-dodecyl-4*H*-dithieno[3,2-*b*:2',3'-*d*]pyrrole-2,6-diyl]-*alt*-[2,3-bis(5-(2-ethylhexyl)thiophen-2-yl)quinoxalin-5,8-diyl]} or PDTPQx.

Stille-L

4-Dodecyl-2,6-bis(trimethylstannyl)-4*H*-dithieno[3,2-*b*:2',3'-*d*]pyrrole (**3**) (148 mg, 0.22 mmol), 5,8-dibromo-2,3-bis(5-(2-ethylhexyl)thiophen-2-yl)quinoxaline (**9**) (149 mg, 0.22 mmol), tris(dibenzylideneacetone)dipalladium(0) (6 mg, 6.6 µmol) and tri(*ortho*-tolyl)phosphine (8 mg, 27 µmol) were dissolved in a mixture of dry toluene (1.6 mL) and dry DMF (0.4 mL), which were degassed with N_2 for 30 min prior to the addition. The resulting mixture was stirred at 120 °C for 19 h, after which the crude polymer material was diluted in chlorobenzene (25 mL). Diethylammonium diethyldithiocarbamate (50 mg) was added and the mixture was stirred at 100 °C for 1 h. The resulting mixture was poured out in methanol, filtered in a thimble, and purified by repetitive Soxhlet extractions using methanol, acetone, *n*-hexanes, and DCM. The DCM fraction obtained from Soxhlet extraction was precipitated in methanol, filtered and dried, yielding a dark green solid (187 mg, 95%). HT-GPC (1,2,4-trichlorobenzene, 160 °C, PS standards): M_n = 12.7 kg/mol, $Đ$ = 2.2. UV-Vis-NIR: $\lambda_{max,film}$ = 756 nm.

Stille-H

4-Dodecyl-2,6-bis(trimethylstannyl)-4*H*-dithieno[3,2-*b*:2',3'-*d*]pyrrole (**3**) (103 mg, 0.15 mmol), 5,8-dibromo-2,3-bis(5-(2-ethylhexyl)thiophen-2-yl)quinoxaline (**9**) (104 mg, 0.15 mmol), tris(dibenzylideneacetone)dipalladium(0) (7 mg, 7.5 µmol) and tri(*ortho*-tolyl)phosphine (9 mg, 30 µmol) was dissolved in a mixture of dry toluene (1.2 mL) and dry DMF (0.3 mL), which were degassed with N_2 for 30 min prior to the addition. The resulting mixture was stirred at 120 °C for 22 h, after which the catalytic system and dry toluene (1.2 mL) were added again. The resulting mixture was stirred at 120 °C for 26 h, after which the crude polymer material was diluted in chlorobenzene (25 mL). Diethylammonium diethyldithiocarbamate (50 mg) was added and the mixture was stirred at 100 °C for 1 h. The resulting mixture was poured out in methanol, filtered in a thimble, and purified by repetitive Soxhlet extractions using methanol, acetone, *n*-hexanes, and DCM. The DCM fraction obtained from Soxhlet extraction was precipitated in methanol, filtered, and dried, yielding a dark green solid (122 mg, 94%). HT-GPC (1,2,4-trichlorobenzene, 160 °C, PS standards): M_n = 27.1 kg/mol, $Đ$ = 2.3. UV-Vis-NIR: $\lambda_{max,film}$ = 756 nm.

DArP

4-Dodecyl-4*H*-dithieno[3,2-*b*:2',3'-*d*]pyrrole (**2**) (104 mg, 0.3 mmol), 5,8-dibromo-2,3-bis(5-(2-ethylhexyl)thiophen-2-yl)quinoxaline (**9**) (203 mg, 0.3 mmol), tris(dibenzylideneacetone)-dipalladium(0) (2.7 mg, 3 µmol), tris(*ortho*-anisyl)phosphine (4.2 mg, 12 µmol), Cs_2CO_3 (293 mg, 0.9 mmol), and pivalic acid (30 mg, 0.3 mmol) were added to a flame-dried Schlenk tube under inert atmosphere. A dry toluene solution of TMEDA (0.375 M; 80 µL, 30 µmol) and 1.2 mL of dry toluene (degassed with N_2 for 30 min prior to the addition) were added. The inert atmosphere was restored, the mixture was stirred at room temperature for 0.5 h and subsequently at 100 °C for 48 h, after which the crude polymer material was diluted in chloroform (25 mL). Diethylammonium diethyldithiocarbamate (50 mg) was added and the mixture was stirred at 60 °C for 1 h. The reaction mixture was cooled to room temperature and washed with water (3 × 15 mL). The organic phase was poured out in methanol, filtered in a thimble, and purified by repetitive Soxhlet extractions using

methanol, acetone, *n*-hexanes, and DCM. The DCM fraction obtained from Soxhlet extraction was precipitated in methanol, filtered, and dried, yielding a dark green solid (223 mg, 86%). HT-GPC (1,2,4-trichlorobenzene, 160 °C, PS standards): M_n = 19.9 kg/mol, $Đ$ = 2.6. UV-Vis-NIR: $\lambda_{max,film}$ = 749 nm.

3. ^{1}H and ^{13}C NMR spectra

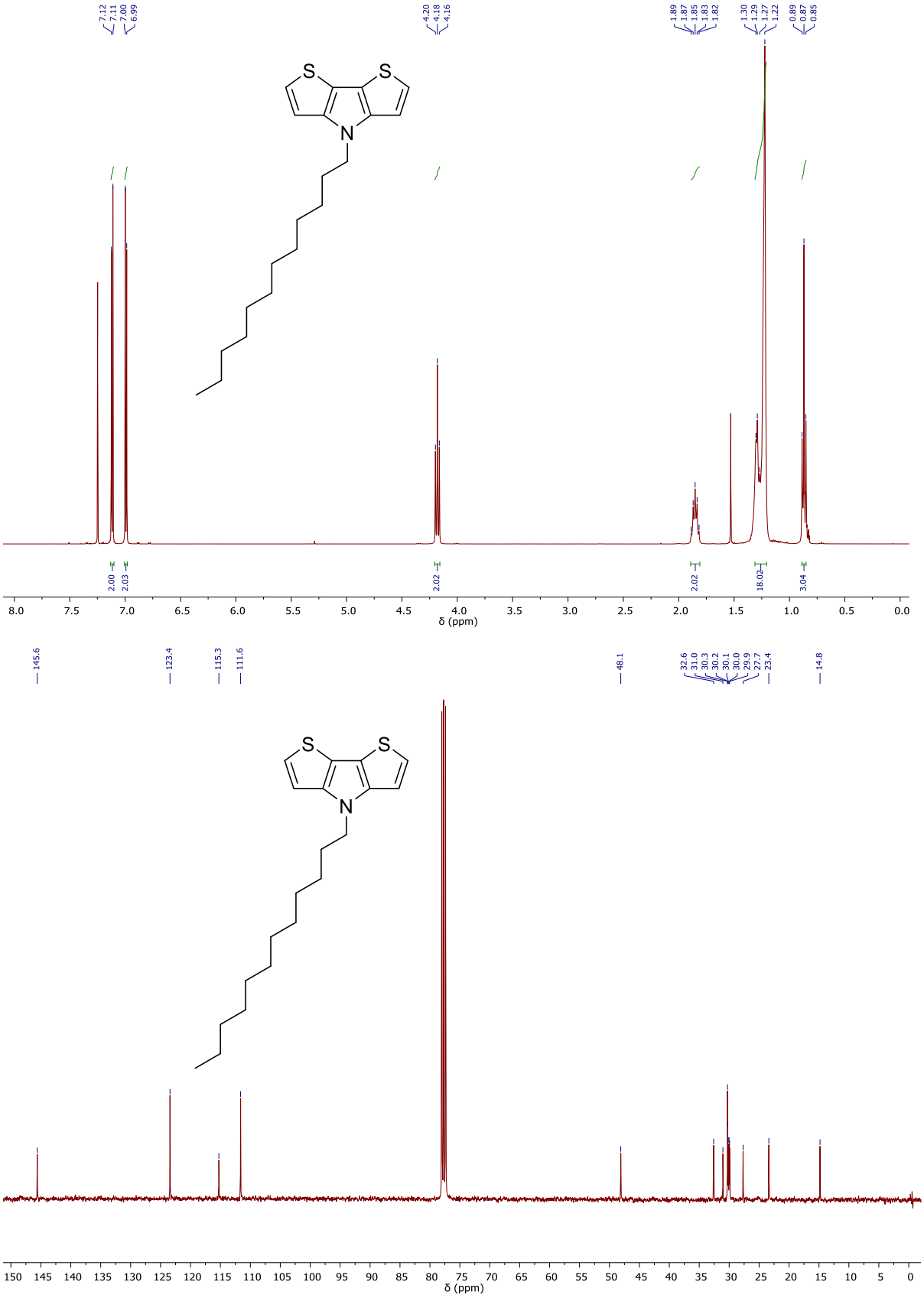

Figure S1 ^{1}H (top) and ^{13}C (bottom) NMR spectra of 4-dodecyl-4*H*-dithieno[3,2-*b*:2',3'-*d*]pyrrole (**2**).

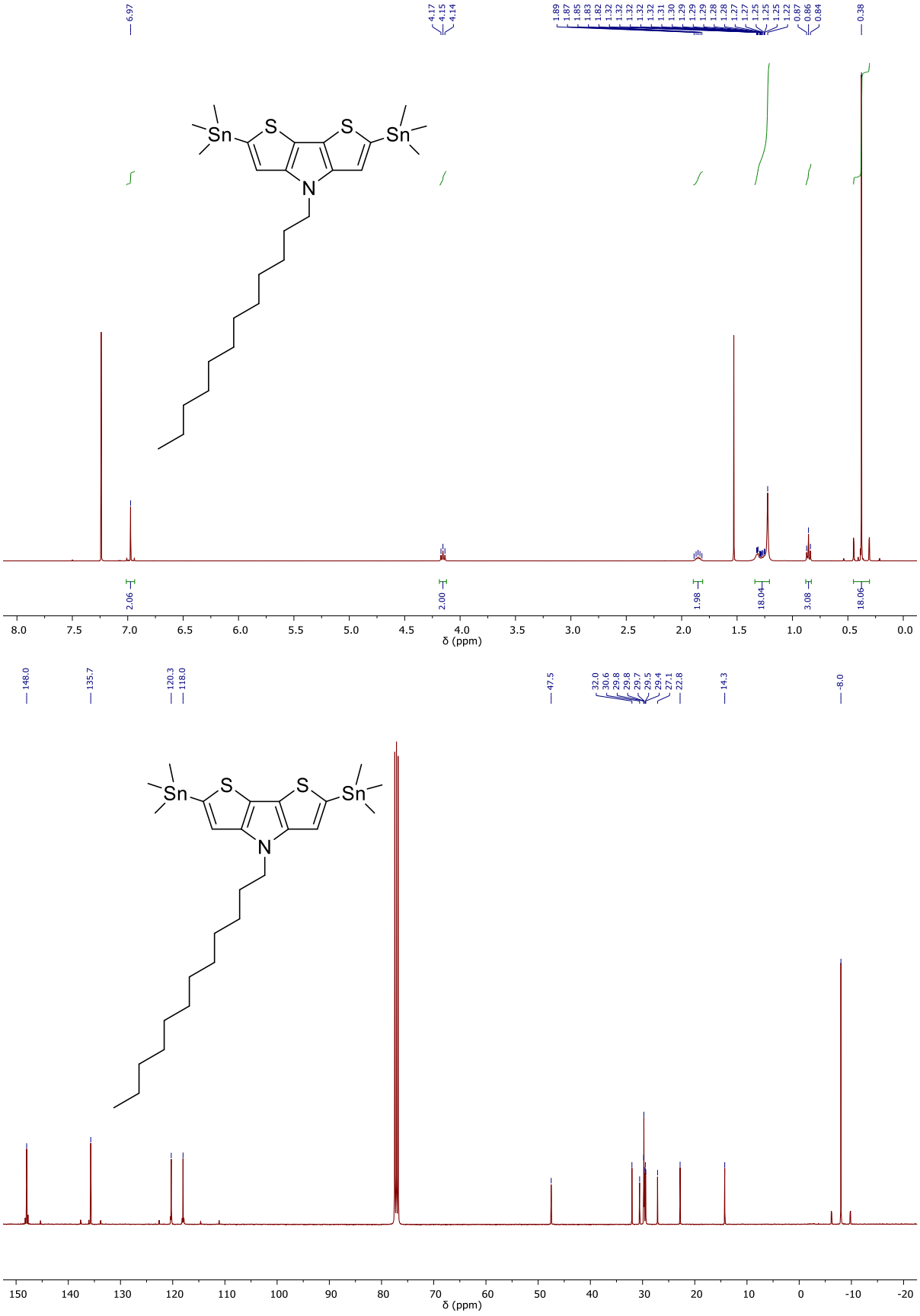

Figure S2 ^{1}H (top) and ^{13}C (bottom) NMR spectra of 4-dodecyl-2,6-bis(trimethylstannyl)-4*H*-dithieno-[3,2-*b*:2',3'-*d*]pyrrole (**3**).

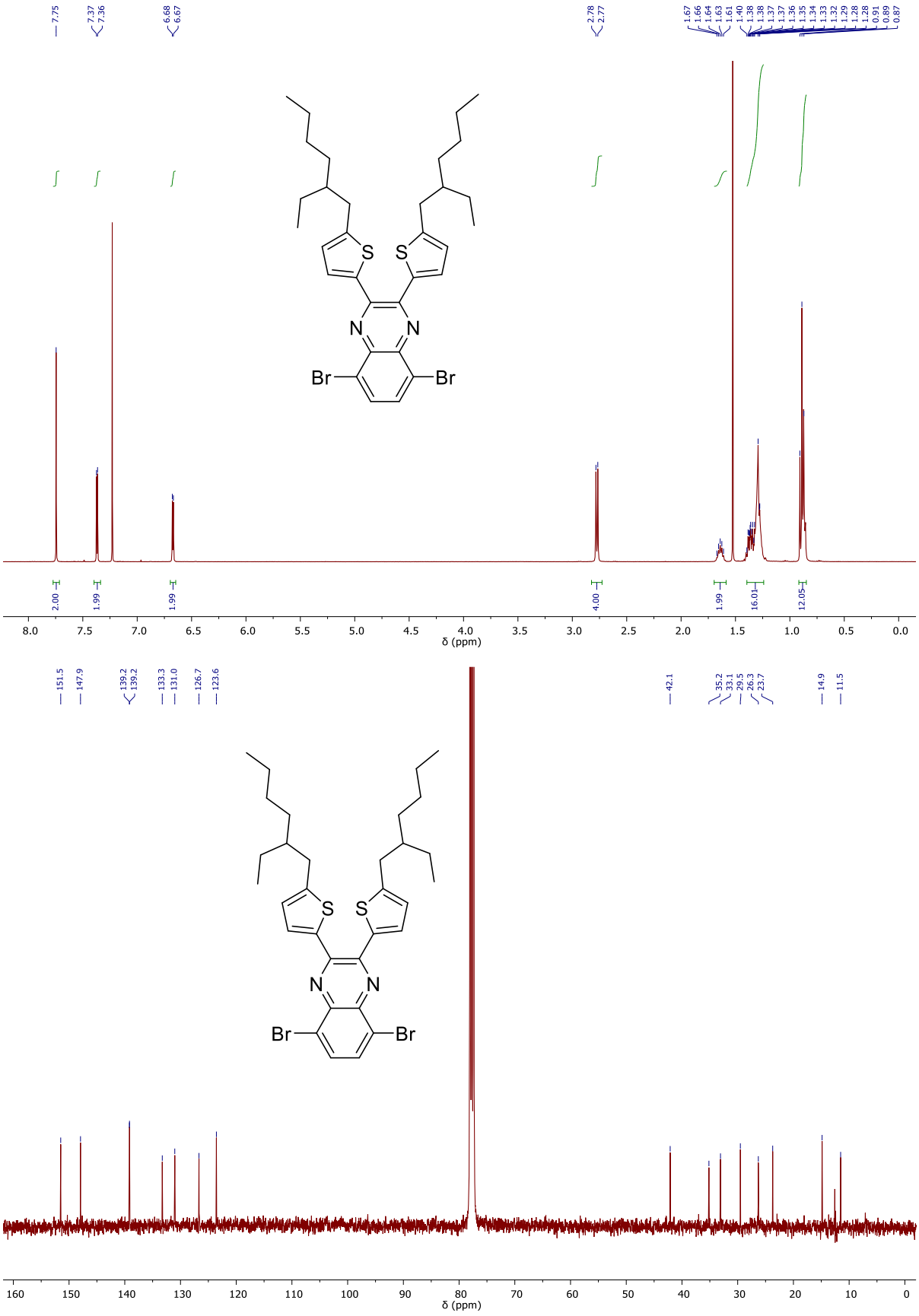

Figure S3 ^{1}H (top) and ^{13}C (bottom) NMR spectra of 5,8-dibromo-2,3-bis(5-(2-ethylhexyl)thiophen-2-yl)quinoxaline (**9**).

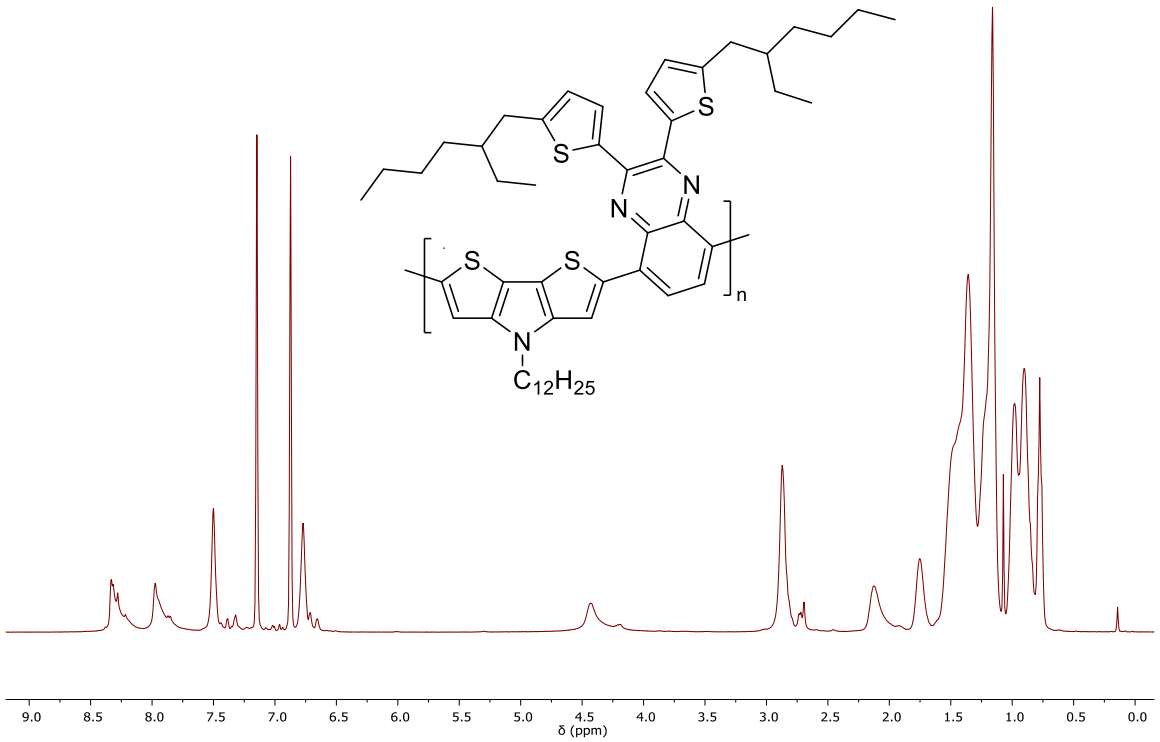

Figure S4 ^{1}H NMR spectrum of the Stille-L PDTPQx polymer.

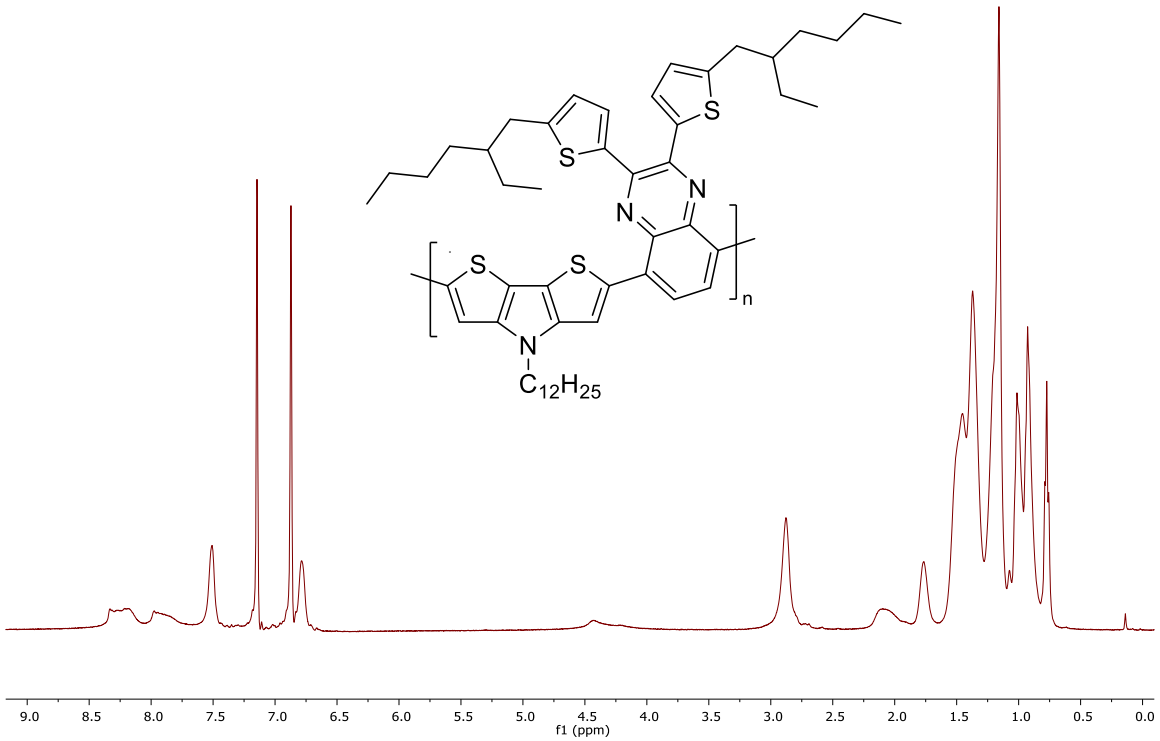

Figure S5 ^{1}H NMR spectrum of the Stille-H PDTPQx polymer.

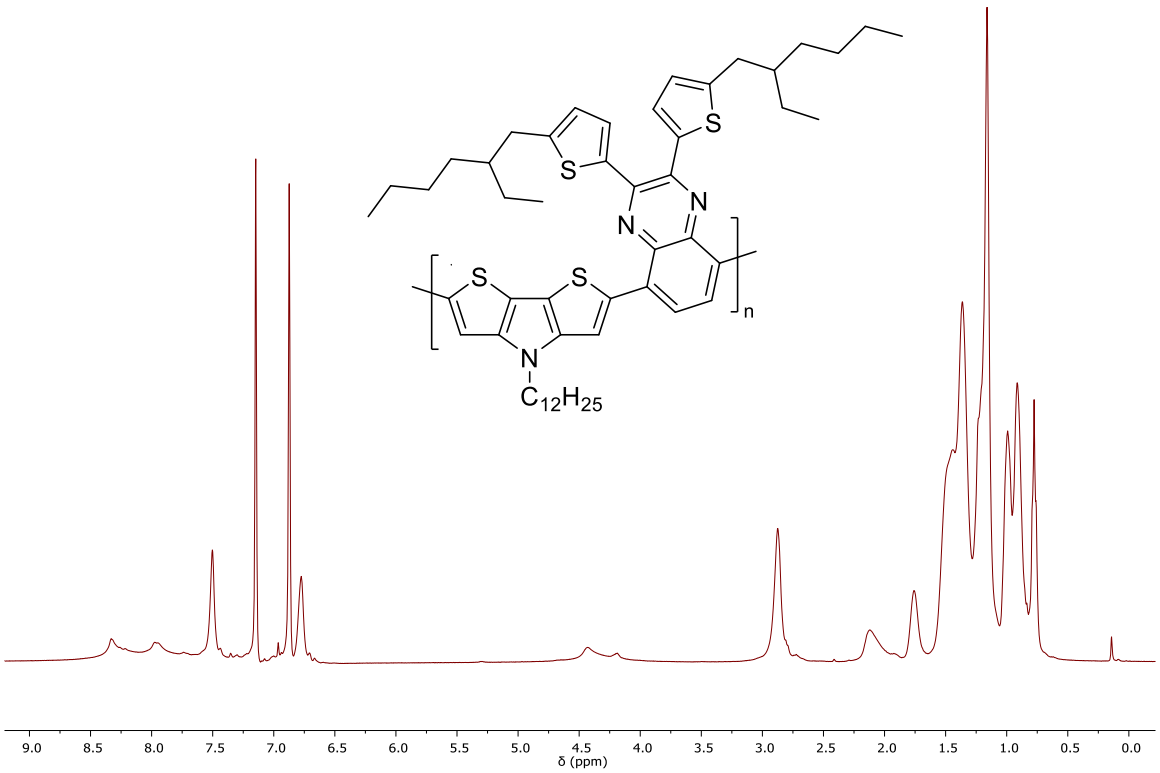

Figure S6 ^{1}H NMR spectrum of the DArP PDTPQx polymer.

4. High-temperature gel permeation chromatography

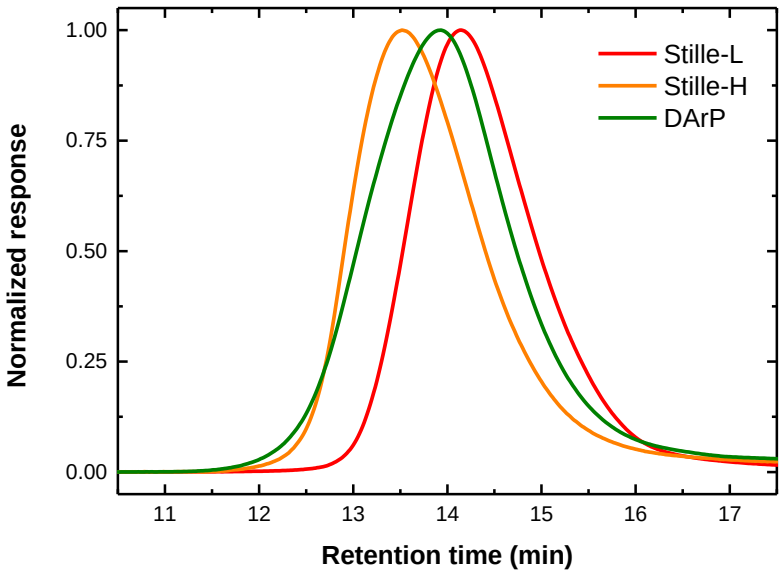

Figure S7 Normalized GPC traces for the PDTPQx polymer series.

5. Cyclic voltammetry

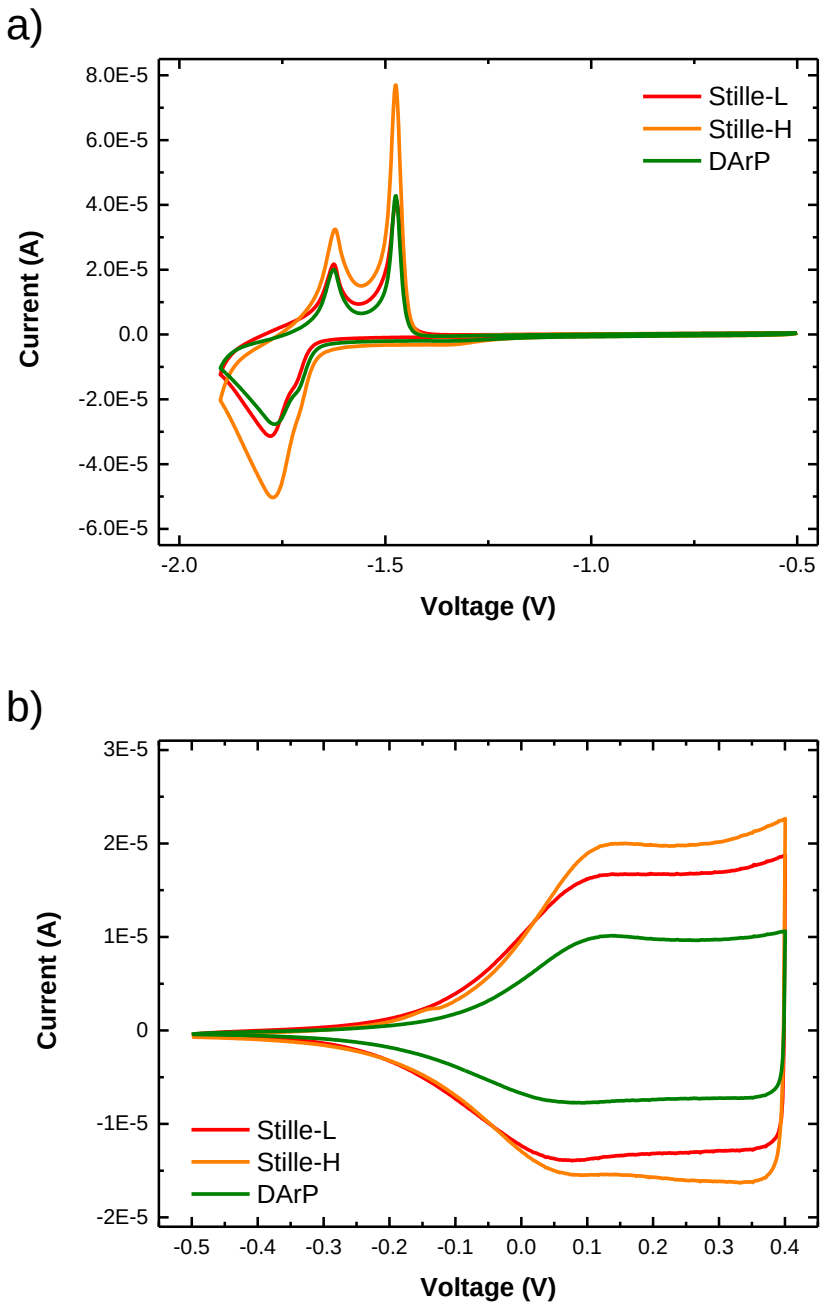

Figure S8 Overlay of the reduction curves (a) and oxidation curves (b) obtained via cyclic voltammetry for the PDTPQx polymer series.

6. UV-Vis-NIR absorption spectroscopy

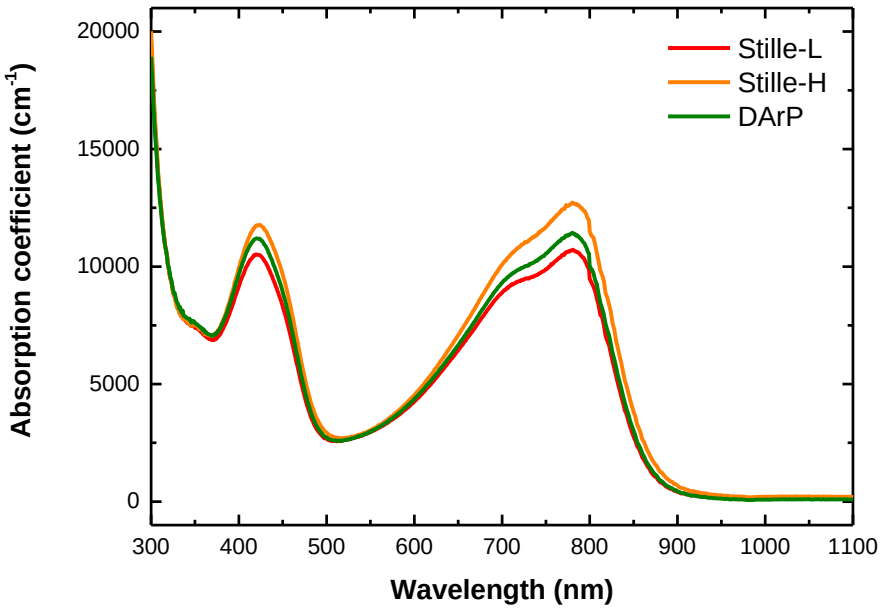

Figure S9 Solid-state UV-Vis-NIR absorption spectra (spin-coated from $CHCl_3$ solution) for the PDTPQx polymer series.

7. Thermal analysis

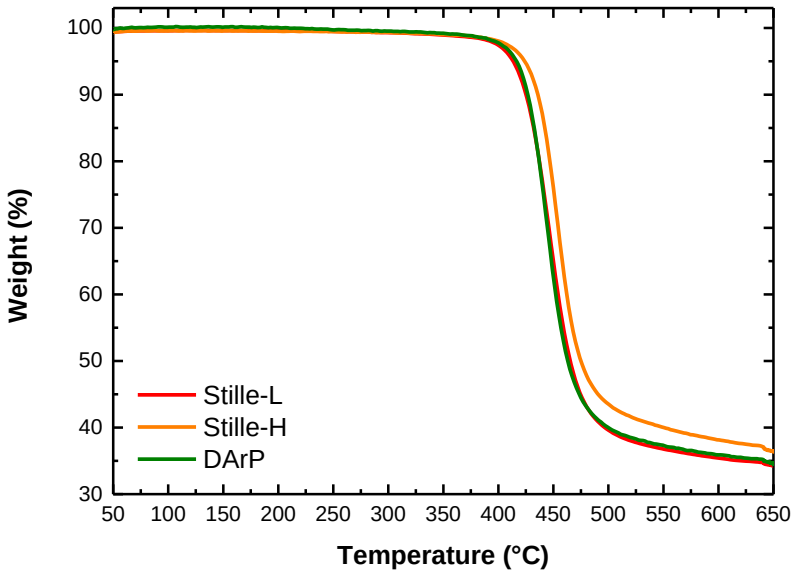

Figure S10 TGA curves depicting the mass loss for the PDTPQx polymer series (while heating at 20 K min^{-1}).

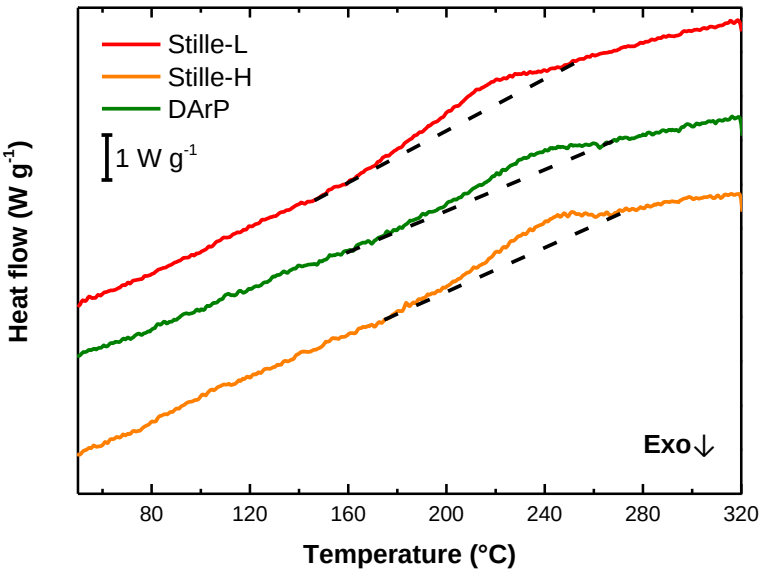

Figure S11 RHC thermograms depicting the second heating for the PDTPQx polymer series at 500 K min^{-1}, after a preceding cooling at 20 K min^{-1}. The curves are shifted vertically for clarity.

8. Organic photodetector fabrication and characterization

Bulk heterojunction organic photodetectors were prepared using the inverted architecture glass/ITO/PEIE/active layer/MoO_3/Ag. The ITO-coated substrates (100 nm, Kintec, sheet resistivity 20 Ω sq^{-1}) were thoroughly cleaned via sonication in soap water, demineralized water, acetone, and isopropanol, followed by a UV/O_3 treatment for 30 min. PEIE [(poly(ethylenimine), 80% ethoxylated solution, 37 wt% in H_2O), Sigma Aldrich] was deposited by spin-coating with a layer thickness of ~5 nm. The PEIE layer was annealed at 100 °C for 10 min. Further processing was performed under nitrogen atmosphere in a glove box (< 1 ppm O_2 and H_2O). The photoactive layer solution, consisting of the active polymers and $PC_{61}BM$ (Solenne), was then spin-coated from chloroform. The optimal PDTPQx:$PC_{61}BM$ ratio was investigated, and the 1:4 ratio was found to be optimal (**Figure S12**). Similar optimization runs with PDTPQx:$PC_{61}BM$ (1:4) were performed for the different photoactive blends (based on the Stille-L, Stille-H, and DArP polymer), for which the data can be found in **Figure S13-S15**. The best performing devices were obtained with a blend solution of PDTPQx:$PC_{61}BM$ (1:4 wt/wt) with a total concentration of 40 mg mL^{-1} in chloroform with addition of 5 v/v% of 1,8-diiodooctane (DIO). The solution was stirred overnight at 60 °C to ensure complete dissolution. The active layer was deposited on top of the PEIE layer by means of spin-coating at room temperature with an optimal layer thickness near 350 nm. Finally, the MoO_3 (10 nm) hole transporting layer and Ag (100 nm) top electrode were sequentially deposited on top of the active layer through a shadow mask by thermal evaporation (< 5 × 10^{-6} mbar) to afford photodetector devices with an active area of 3 mm^2. Performance parameters of the optimized OPDs at peak detectivity are shown in **Table S1**. The cavity OPDs were fabricated using the inverted device structure Eagle XG glass/Au(1.5 nm)/Ag(28 nm)/PEIE/active layer/MoO_3/Ag. The semi-transparent thin Ag films were fabricated by thermal evaporation (< 5 × 10^{-6} mbar) with an extremely thin Au seed layer beneath.[6] The deposition rate for Au and Ag was 0.5 and 4 Å s^{-1}, respectively. All other parameters for the cavity OPDs were equal to the regular OPDs. Performance parameters of the organic resonant cavity photodetectors at resonance wavelengths are shown in **Table S2**. The freshly fabricated devices were measured in an inert atmosphere and light and dark $J-V$ curves (forward scan with a step of 25 mV) were recorded using a Keithley 2400 Source Meter under AM1.5 1-sun illumination, provided by a solar simulator (Newport 91195A) with a silicon calibrated intensity equivalent to 100 mW cm^{-2}, and under dark, respectively. The EQE_{PV} spectrum for each cell was measured under chopped (123 Hz) monochromatic illumination from a Xe lamp (100 W, Newport) modulated by a Newport Cornerstone™ 130° Monochromator and an optical wheel chopper. The generated photocurrent from the solar cells was amplified with a Stanford Research System Model SR830 lock-in amplifier, and a calibrated silicon FDS100-CAL photodiode was employed as a reference cell. For the sensitive EQE measurements, an INVENIO R (Bruker Optics) with an external detector was employed. A low-noise current amplifier was used to amplify the photocurrent generated under illumination of the devices, with the illumination light modulated by the Fourier-transform infrared (FTIR) setup. The blend thickness was monitored by a Bruker Veeco Dektak XT profilometer. Atomic force microscopy (AFM) experiments were performed (on the devices used for the $J-V$ measurements) with a JPK NanoWizard 3 AFM (JPK Instruments AG, Berlin, Germany) using AC mode in air. Silicon ACTA-50 tips from AppNano with cantilever length ~125 mm, spring constant ~40 N m^{-1} and resonance frequency ~300 kHz were used. The scan angle, set point height, gain values, and scan rate were adjusted according to the calibration of the AFM tip. The transmission electron microscopy (TEM) study on the freestanding polymer films (thickness around 300 to 400 nm) was performed with a FEI Tecnai Spirit Twin using an accelerating voltage of 120 kV for the electrons. The Bright Field (BF) images and diffraction patterns were recorded with an Eagle 4kx4k CCD camera under binning 4 conditions.

9. Organic photodetector optimization

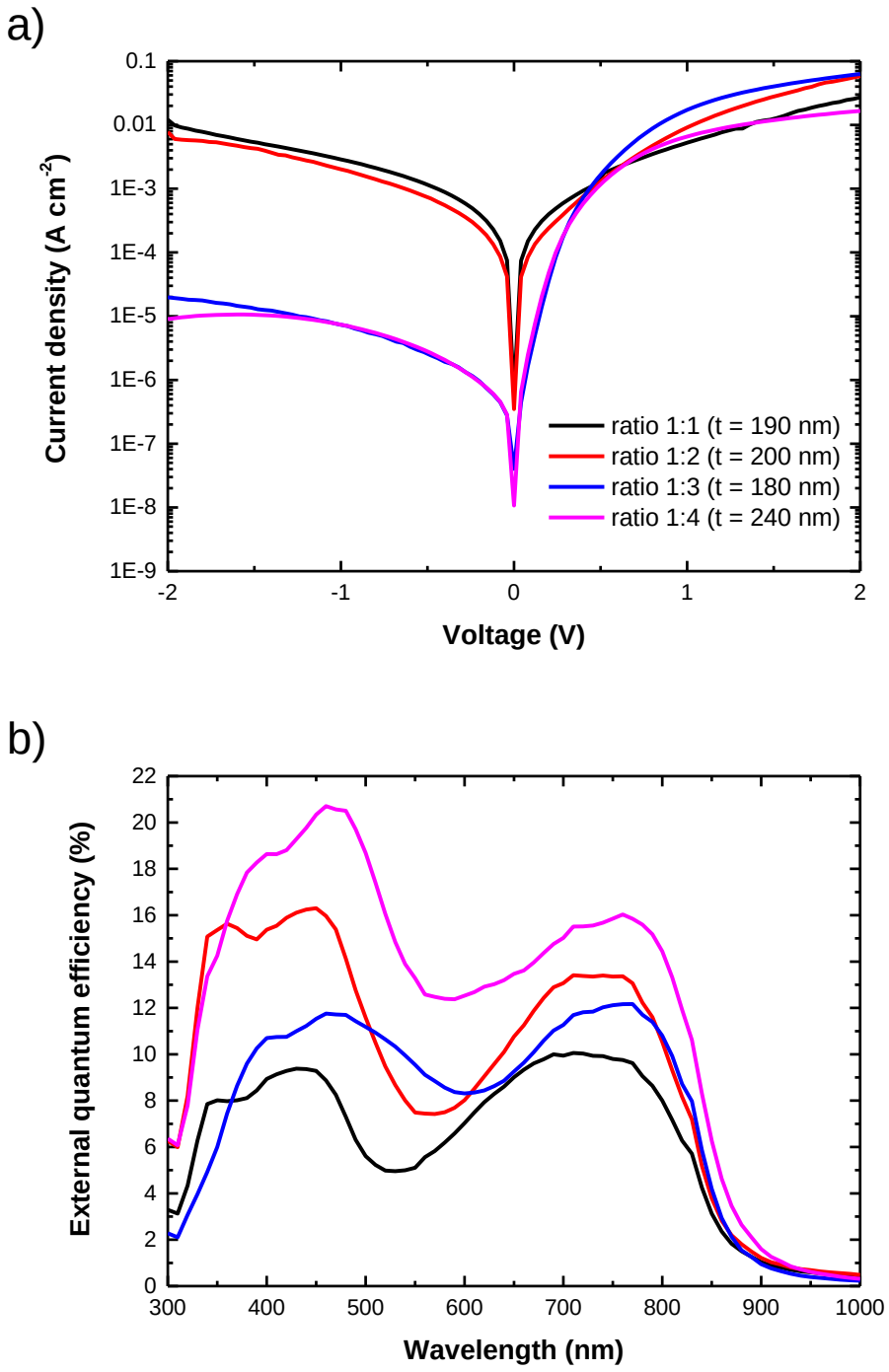

Figure S12 Organic photodetector optimization of the polymer:$PC_{61}BM$ ratio, based on the DArP polymer and spin-coated from chloroform: (a) $J-V$ curves, measured in the dark. (b) EQE spectra, measured at 0 V. Active layer blend thicknesses (t) are given in the legend.

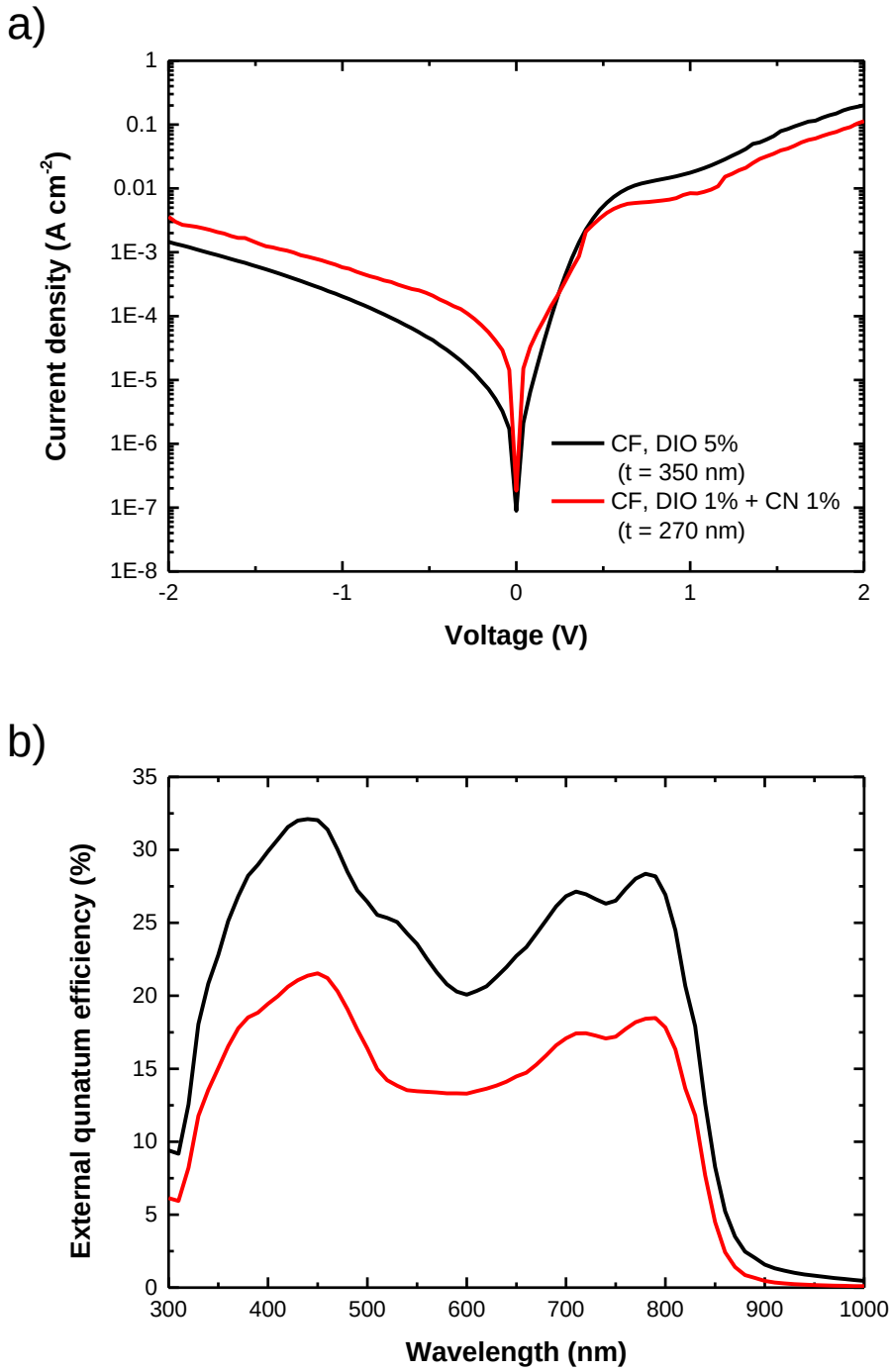

Figure S13 Organic photodetector optimization with solvent additives for the PDTPQx:$PC_{61}BM$ (1:4) devices based on the Stille-L polymer: (a) $J-V$ curves, measured in the dark. (b) EQE spectra, measured at 0 V. Systematically short-circuited devices are not shown. Active layer blend thicknesses (t) are given in the legend (CF = chloroform, CN = 1-chloronaphthalene, DIO = 1,8-diiodooctane).

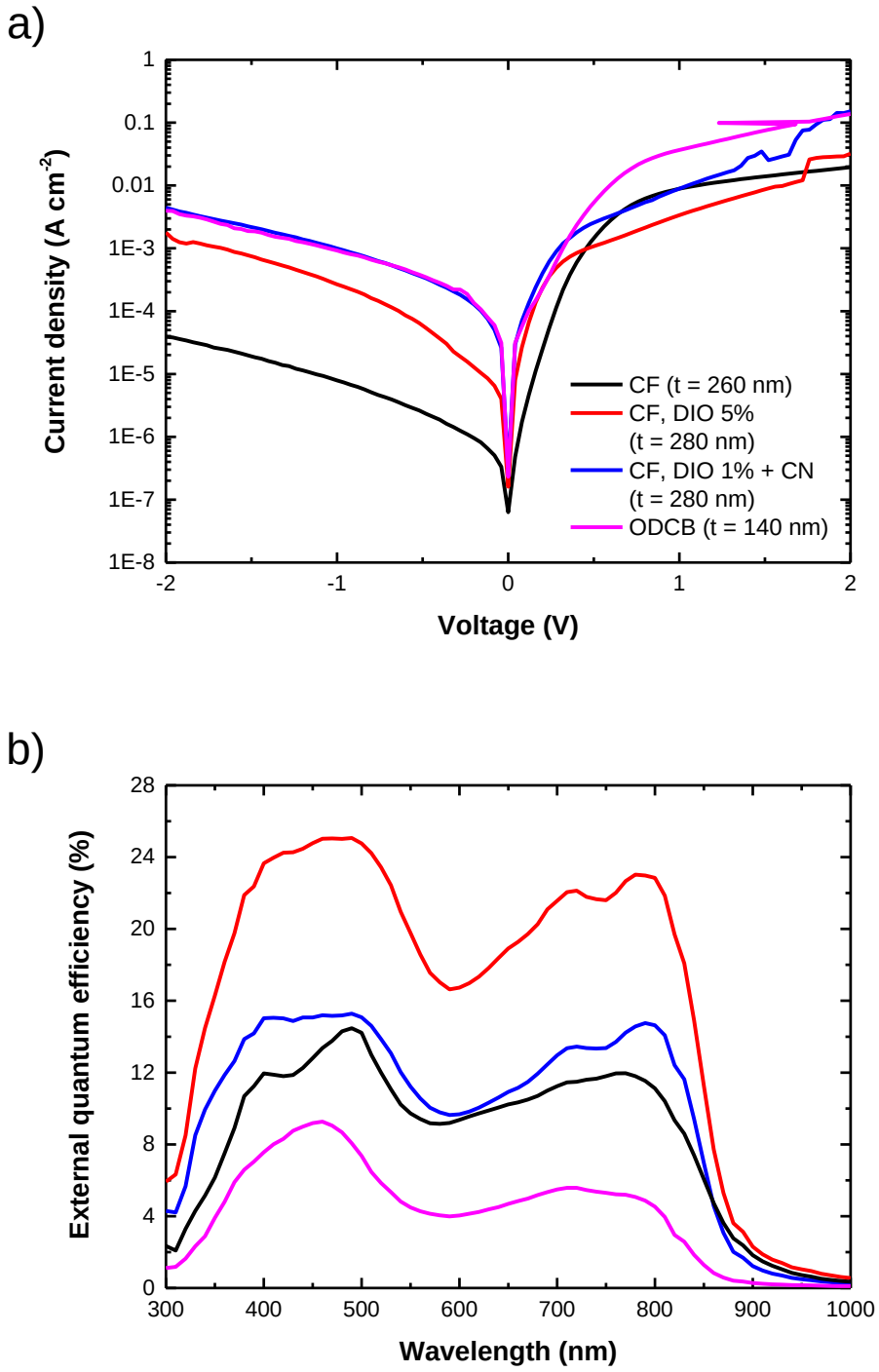

Figure S14 Organic photodetector optimization with solvent additives for the PDTPQx:$PC_{61}BM$ (1:4) devices based on the Stille-H polymer: (a) $J-V$ curves, measured in the dark. (b) EQE spectra, measured at 0 V. Systematically short-circuited devices are not shown. Active layer blend thicknesses (t) are given in the legend (CF = chloroform, ODCB = *ortho*-dichlorobenzene, CN = 1-chloronaphthalene, DIO = 1,8-diiodooctane).

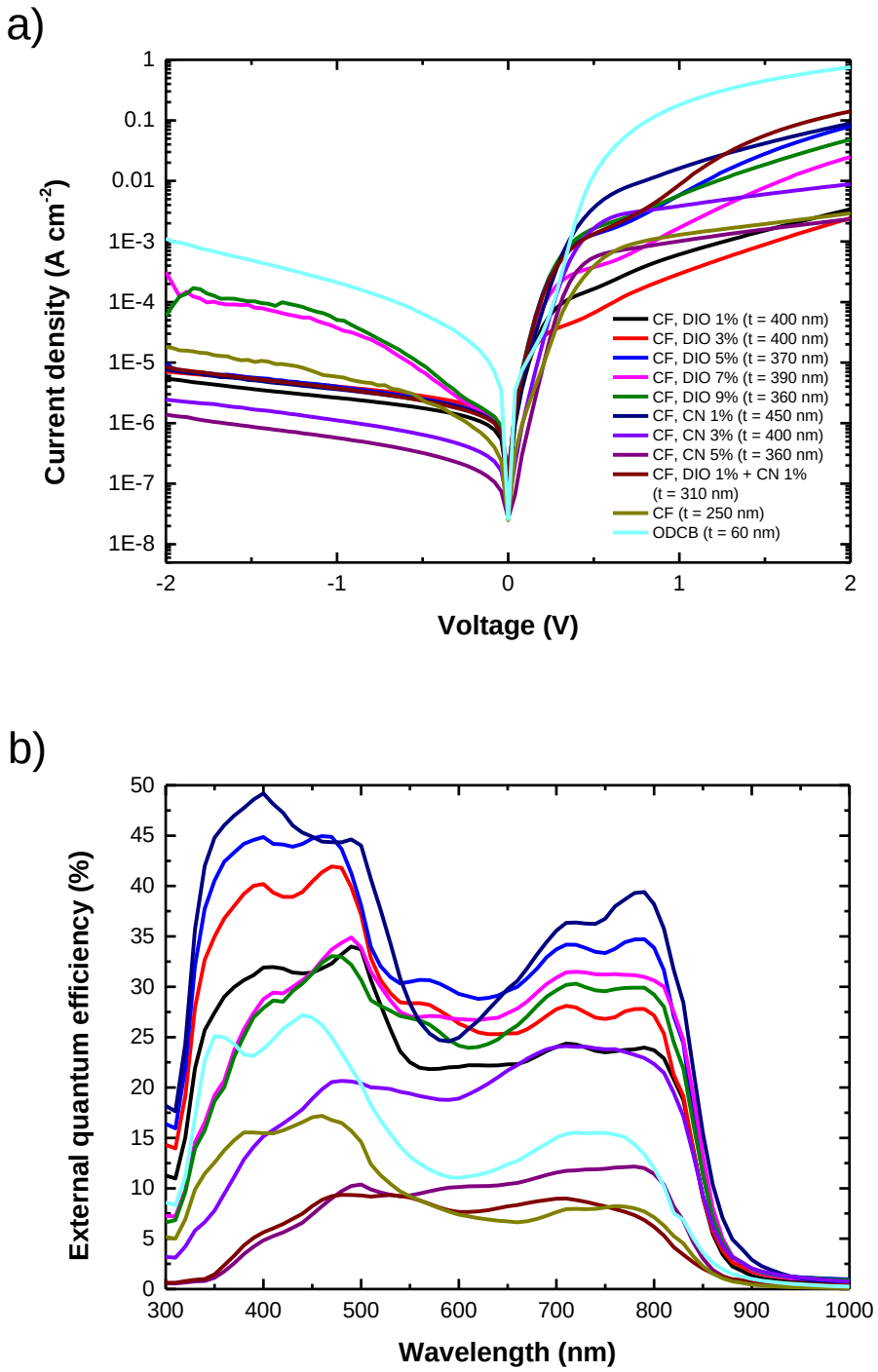

Figure S15 Organic photodetector optimization with solvent additives for the PDTPQx:$PC_{61}BM$ (1:4) devices based on the DArP polymer: (a) $J - V$ curves, measured in the dark. (b) EQE spectra, measured at 0 V. Systematically short-circuited devices are not shown. Active layer blend thicknesses (t) are given in the legend (CF = chloroform, ODCB = *ortho*-dichlorobenzene, CN = 1-chloronaphthalene, DIO = 1,8-diiodooctane).

Table S1 Performance parameters for the optimized OPDs at peak detectivity, based on the Stille-L, Stille-H, and DArP polymer batches.

Material	Bias (V)	Wavelength (nm)	EQE (%)	Responsivity (A W^{-1})	J_D (A cm^{-2})	R_{sh} (Ω cm^2)	D^* (Jones)
Stille-L	-0.1	790	28.2	0.18	2.40×10^{-6}	4.74×10^{4}	1.70×10^{11}
Stille-H	-0.1	800	22.8	0.15	6.98×10^{-6}	1.62×10^{5}	9.64×10^{10}
DArP	-0.1	790	34.7	0.22	1.32×10^{-6}	2.18×10^{5}	3.14×10^{11}
DArP	-2	800	35.2	0.23	9.71×10^{-6}	2.18×10^{5}	1.27×10^{10}

Table S2 Performance parameters for the organic resonant cavity photodetectors at the resonance wavelengths.

Material	Bias (V)	Wavelength (nm)	EQE (%)	Responsivity (A W^{-1})	J_D (A cm^{-2})	R_{sh} (Ω cm^2)	D^* (Jones)
DArP	-0.1	1016.4	2.5	2.06×10^{-2}	1.78×10^{-6}	6.01×10^{4}	2.24×10^{10}
DArP	-0.1	1140.5	1.0	9.46×10^{-3}	1.68×10^{-6}	6.44×10^{4}	1.06×10^{10}

10. Atomic force microscopy (AFM)

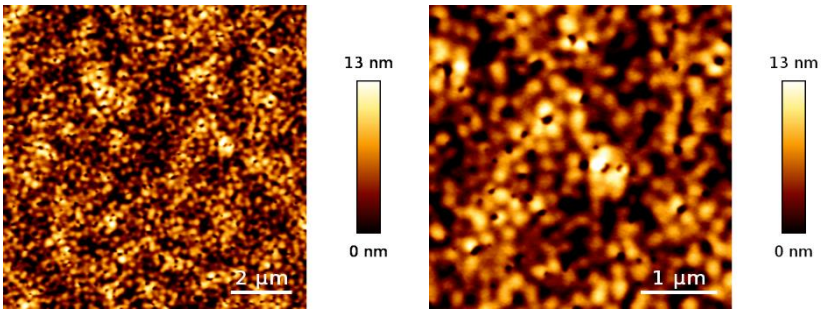

Figure S16 AFM images of a PDTPQx:$PC_{61}BM$ (1:4) active layer based on the Stille-L polymer batch, processed without solvent additive.

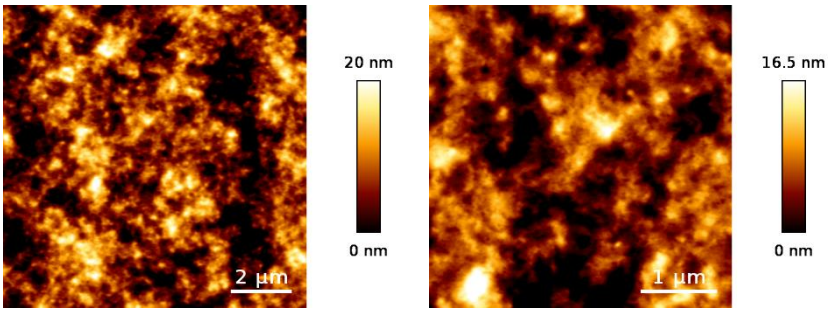

Figure S17 AFM images of a PDTPQx:$PC_{61}BM$ (1:4) active layer based on the Stille-L polymer batch, processed with the solvent additive DIO (5 v/v%).

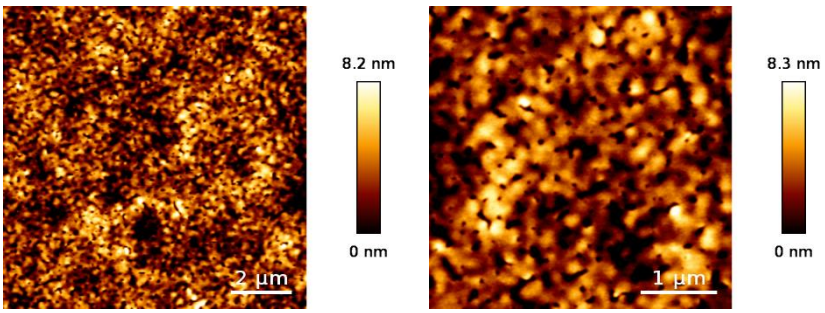

Figure S18 AFM images of a PDTPQx:$PC_{61}BM$ (1:4) active layer based on the Stille-H polymer batch, processed without solvent additive.

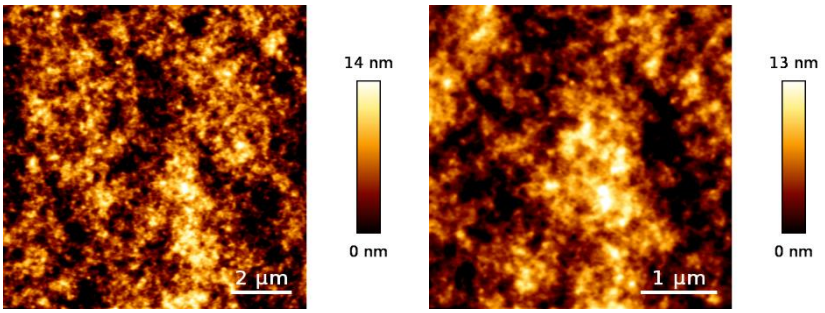

Figure S19 AFM images of a PDTPQx:$PC_{61}BM$ (1:4) active layer based on the Stille-H polymer batch, processed with the solvent additive DIO (5 v/v%).

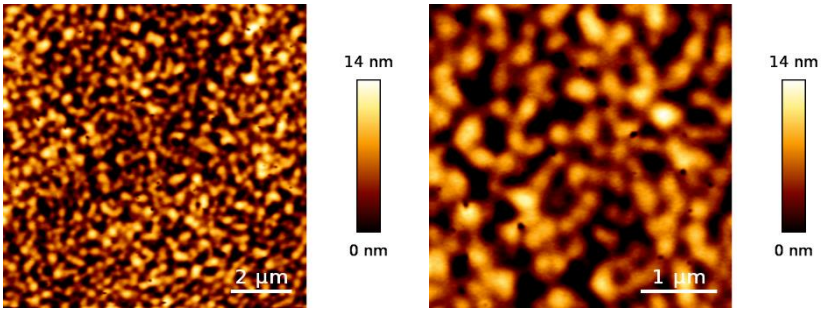

Figure S20 AFM images of a PDTPQx:$PC_{61}BM$ (1:4) active layer based on the DArP polymer batch, processed without solvent additive.

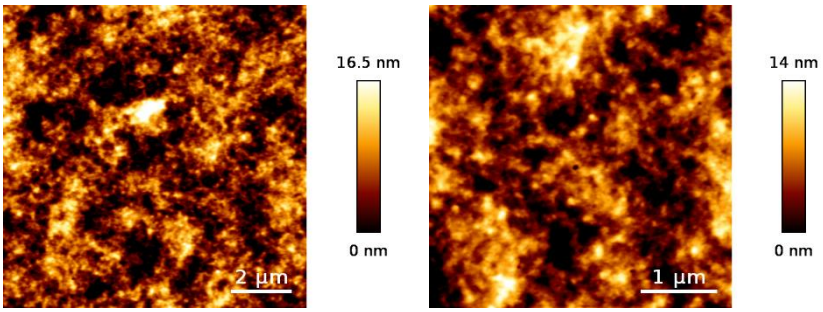

Figure S21 AFM images of a PDTPQx:$PC_{61}BM$ (1:4) active layer based on the DArP polymer batch, processed with the solvent additive DIO (5 v/v%).

11. Transmission electron microscopy (TEM)

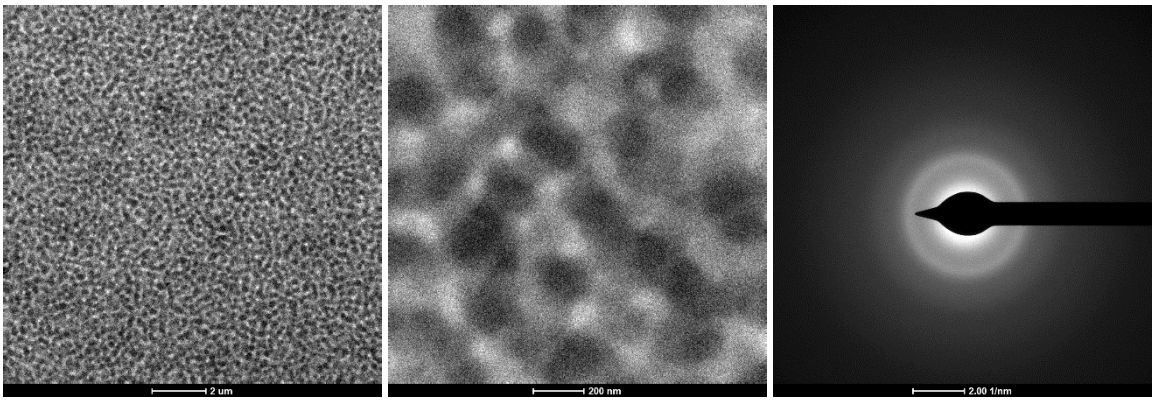

Figure S22 TEM images of a PDTPQx:$PC_{61}BM$ (1:4) active layer based on the Stille-L batch, processed without solvent additive.

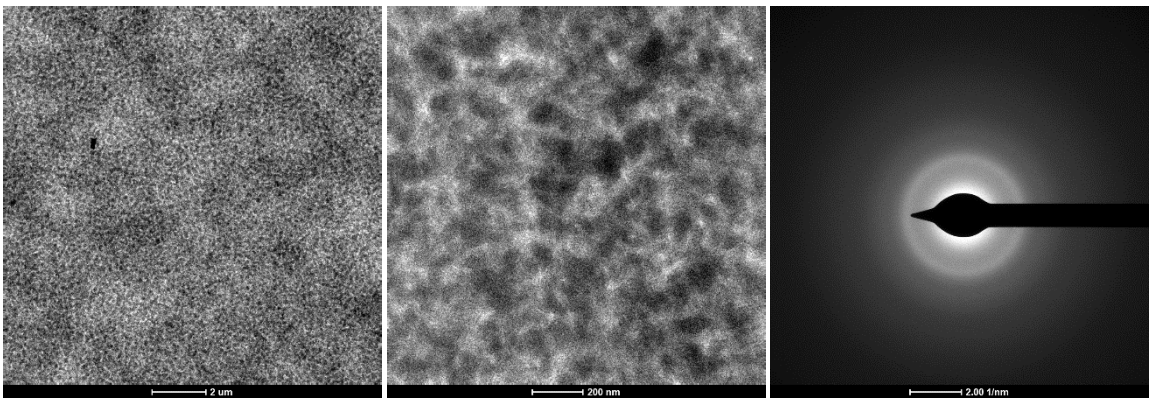

Figure S23 TEM images of a PDTPQx:$PC_{61}BM$ (1:4) active layer based on the Stille-L polymer batch, processed with the solvent additive DIO (5 v/v%).

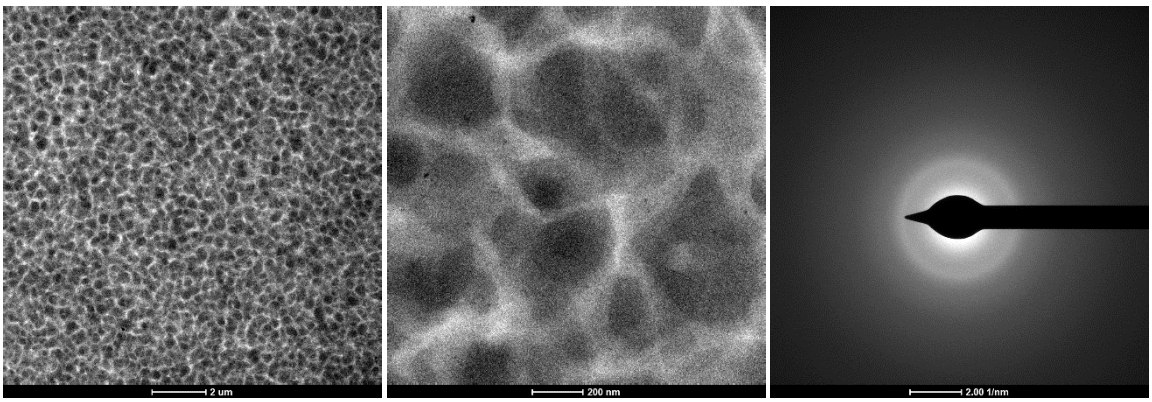

Figure S24 TEM images of a PDTPQx:$PC_{61}BM$ (1:4) active layer based on the Stille-H polymer batch, processed without solvent additive.

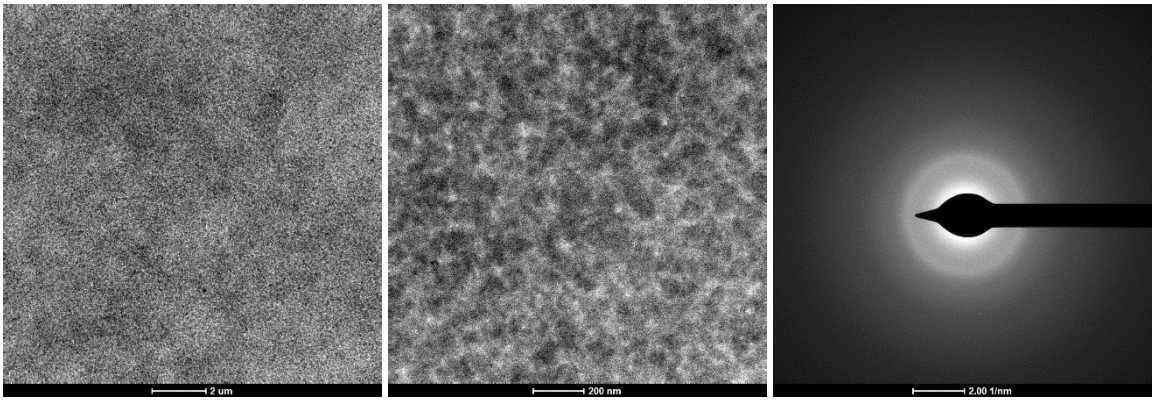

Figure S25 TEM images of a PDTPQx:$PC_{61}BM$ (1:4) active layer based on the Stille-H polymer batch, processed with the solvent additive DIO (5 v/v%).

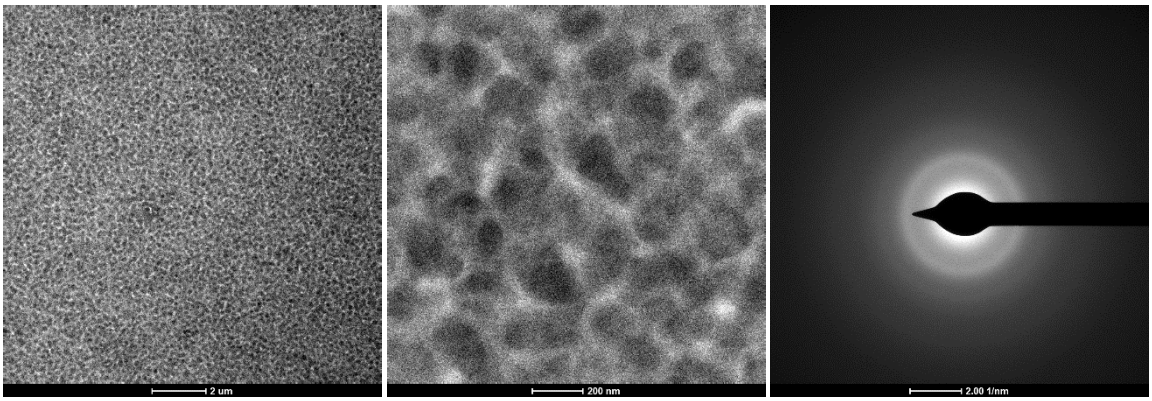

Figure S26 TEM images of a PDTPQx:$PC_{61}BM$ (1:4) active layer based on the DArP polymer batch, processed without solvent additive.

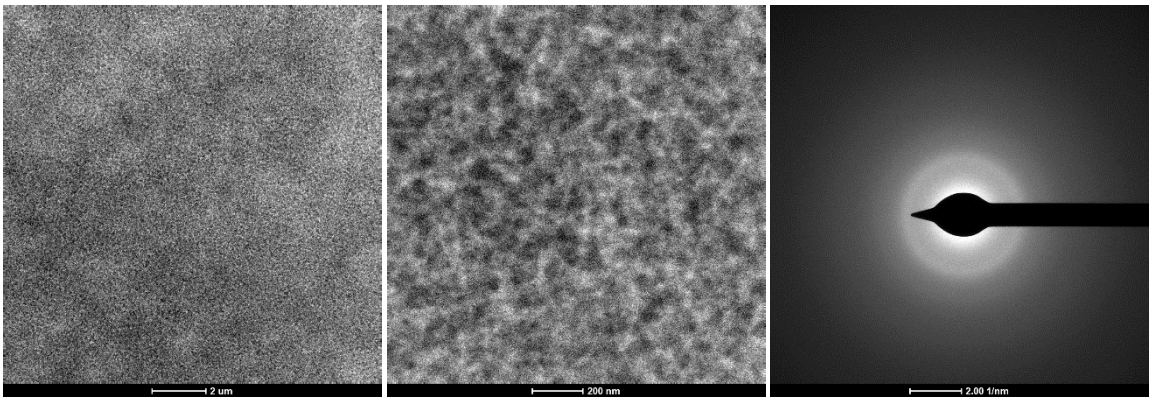

Figure S27 TEM images of a PDTPQx:$PC_{61}BM$ (1:4) active layer based on the DArP polymer batch, processed with the solvent additive DIO (5 v/v%).

12. Photoluminescence spectroscopy

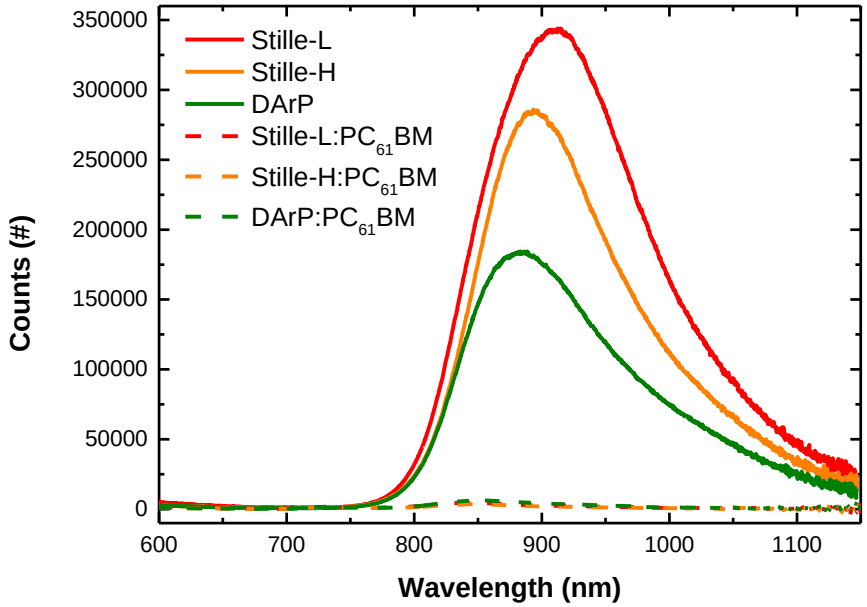

Figure S28 Photoluminescence spectra for the pure PDTPQx polymer films and the PDTPQx:$PC_{61}BM$ (1:4) blends.

13. References

1. Trasatti, S., The absolute electrode potential: an explanatory note (Recommendations 1986). *Pure and Applied Chemistry* **1986,** *58*, 955-966.
2. Bard, A. J.; Faulkner, L. R., Fundamentals and applications. *Electrochemical methods* **2001,** *2*, 580-632.
3. Mishra, S. P.; Palai, A. K.; Srivastava, R.; Kamalasanan, M. N.; Patri, M., Dithieno[3,2-b:2′,3′-d]pyrrole–alkylthiophene–benzo[c][1,2,5]thiadiazole-based highly stable and low band gap polymers for polymer light-emitting diodes. *Journal of Polymer Science Part A: Polymer Chemistry* **2009,** *47*, 6514-6525.
4. Marin, L.; Lutsen, L.; Vanderzande, D.; Maes, W., Quinoxaline derivatives with broadened absorption patterns. *Organic & Biomolecular Chemistry* **2013,** *11*, 5866-5876.
5. Naef, R.; Balli, H., Synthesis, Structure and Photochemical Properties of 4, 4′, 7, 7′-Tetra-substituted 1,1′, 3,3′-Tetraethylbenzimidazolotriazatrimethine Cyanines. *Helvetica Chimica Acta* **1978,** *61*, 2958-2973.
6. Liu, Q.; Gerling, L. G.; Bernal-Texca, F.; Toudert, J.; Li, T.; Zhan, X.; Martorell, J., Light Harvesting at Oblique Incidence Decoupled from Transmission in Organic Solar Cells Exhibiting 9.8% Efficiency and 50% Visible Light Transparency. *Advanced Energy Materials* **2020,** *10*, 1904196.